

DESIGN AND FABRICATION OF GaN-BASED HETEROJUNCTION
BIPOLAR TRANSISTORS

By

KYU-PIL LEE

A DISSERTATION PRESENTED TO THE GRADUATE SCHOOL
OF THE UNIVERSITY OF FLORIDA IN PARTIAL FULFILLMENT
OF THE REQUIREMENTS FOR THE DEGREE OF
DOCTOR OF PHILOSOPHY

UNIVERSITY OF FLORIDA

2003

To my wife Soon-Hee Hong

In his heart a man plans his course,
But, the LORD determines his steps.

Proverbs 16:9

ACKNOWLEDGMENTS

First and foremost, I would like to express great appreciation with all my heart to Professor Pearton and Professor Ren for their expert advice, guidance, and instruction throughout the research. I also give special thanks to members of my committee (Professor Abernathy, Professor Norton, and Professor Singh) for their professional input and support. Additional special thanks are reserved for the people of our research group (Kwang-hyun, Kelly, Ben, Jihyun, and Risarbh) for their assistance, care, and friendship. I am very grateful to past group members (Sirichai, Pil-yeon, David, Donald and Bee). I also give my thanks to P. Mathis for her endless help and kindness; and to Mr. Santiago who is network assistant in the Chemical Engineering Department, because of his great help with my simulation. I also thank my discussion partners about material growth technologies, Dr. B. Gila, Dr. M. Overberg, Jerry and Dr. Kang-Nyung Lee. I would like to give my thanks to my friends (especially Kyung-hoon, Young-woo, Se-jin, Byeng-sung, Yong-wook, and Hyeng-jin). Even when they were very busy, they always helped my research work without hesitation.

I cannot forget Samsung's vice president Dr. Jong-woo Park's devoted help, and the steadfast support from Samsung Electronics. Without Samsung's financial support, it would not have been easy to finish my work successfully at the University of Florida.

I give all of my sincere gratitude to my parents, my parents-in-law, and my brothers and sisters. I especially thank my lovely wife, Soon-hee; my smart son,

Ah-rhem-sol; and my honey-sweet daughter, Ah-rhem-byeol, for their emotional help, inspiration, and continual prayers. Finally, I thank our Jesus.

TABLE OF CONTENTS

	<u>page</u>
ACKNOWLEDGMENTS	iii
LIST OF TABLES	vii
LIST OF FIGURES.....	viii
ABSTRACT.....	xiii
 CHAPTER	
1 INTRODUCTION.....	1
2 LITERATURE REVIEW	7
2.1 GaN-Based Material Characteristics	7
2.1.1 Physical Properties	7
2.1.2 Transport Properties	13
2.1.2.1 Electron Saturation Velocity	13
2.1.2.2 Mobility Versus Impurities / Phonons	14
2.1.2.3 Mobility Versus Dislocation.....	16
2.1.2.4 Minority Carrier Lifetimes	17
2.1.3 Physical Parameters of III-Nitride Semiconductors.....	17
2.2 Simulation	20
2.2.1 Device Simulators	21
2.2.1.1 MEDICI	22
2.2.1.2 ATLAS	25
2.2.1.3 MINIMOS-NT	25
2.2.1.4 PISCES-2ET	26
2.2.1.5 SEDAN	27
2.2.2 Basic Equations	28
2.3 GaN-Based Electronic Devices	30
2.3.1 Field Effect Transistors (FETs).....	31
2.3.1.1 Heterojunction Field Effect Transistors	32
2.3.1.2 GaN-based MOSFETs.....	35
2.3.2 GaN-Based Bipolar Devices	36
2.3.2.1 Physics of Heterojunction Bipolar Transistors	37

3	PROCESS DEVELOPMENT FOR GaN-BASED BIBOLAR TRANSISORS	41
3.1	Introduction	41
3.2	Process Development for Small-Area GaN-Based Bipolar Transistors	42
3.2.1	Experimental Methods	42
3.2.2	Results and Discussion	42
3.2.2.1	Development of Self-Aligned Process	42
3.2.2.2	Temperature Dependent Performance of GaN-Based HBTs.....	54
3.2.2.3	Emitter-and Base-Regrowth GaN-Based HBTs and BJTs	58
4	SIMULATION OF GaN-BASED NPN BIPOLAR TANSISTORS	63
4.1	Introduction	63
4.2	Effects of Base Structure on Performance of Gan-Based Heterojunction Bipolar Transistors.....	63
4.2.1	Experimental Methods	63
4.2.2	Results and Discussion	67
4.3	Influence of Layer Doping and Thickness on Predicted Performance of npn AlGaIn/GaN HBTs	75
4.3.1	Experimental Methods	75
4.3.2	Results and Discussion	75
4.4	Simulations of InGaIn-Base Heterojunction Bipolar Transistors	87
4.4.2	Experimental Methods	87
4.4.2	Results and Discussion	88
4.5	Rf Performance of GaN-Based npn Bipolar Transistors	99
4.5.1	Experimental Methods	99
4.5.2	Results and Discussion	100
5	SIMULATION OF GaN-BASED PNP BIPOLAR TRANSISTORS	112
5.1	Introduction	112
5.2	Temperature Dependence of pnp GaN/InGaIn HBT Performance	112
5.2.1	Experimental Methods.....	112
5.2.2	Results and Discussion	114
6	SUMMARY	122
	REFERENCES	125
	BIOGRAPHICAL SKETCH	131

LIST OF TABLES

<u>Table</u>	<u>page</u>
2-1. The physical parameters in different semiconductor materials.....	8
2-2. Ionization energy of impurities for WurtziteGaN.....	9
2-3. Physical parameters of III-Nitride semiconductors.....	18
2-4. Comparison of different device simulators.....	23
2-5. Naming conventions of the frequency band.....	34
2-6. Band discontinuities at heterointerfaces	39
3-1. Temperature-dependent contact data for p-GaN.....	56
4-1. Working condition of devices as process design	67
4-2. Base current components for different base structures	69
4-3. Base current components as base doping.....	71
4-4. Base current components as a function of emitter doping	73

LIST OF FIGURES

<u>Figure</u>	<u>page</u>
2-1 The III-V compound semiconductor tree	7
2-2 SIMS profile of Mg tail in emitter of MOCVD grown npn structure compared with MBE grown junctions	11
2-3 Contributions to electron mobility in GaN from polar optical, piezoelectric and acoustics scattering, as a function of temperature	14
2-4 Effect of ionized impurity scattering on electron mobility in GaN for total ionized impurity concentration of $7.5 \times 10^{16} \text{ cm}^{-3}$, and carrier densities of (1) $5 \times 10^{17} \text{ cm}^{-3}$; (2) $2 \times 10^{17} \text{ cm}^{-3}$; (3) $7.5 \times 10^{16} \text{ cm}^{-3}$; (4) $2 \times 10^{16} \text{ cm}^{-3}$	15
2-5 Electron mobilities in cubic (dashed line) and hexagonal (solid line) GaN	16
2-6 Schematic structure of HEMT	33
2-7 Schematic structure of MOSFET	36
2-8 Basic features of energy band diagram of HBT	38
2-9 Various current components in a HBT.	38
3-1 Mask layout of the small size HBT	43
3-2 Process sequence for HBT to the emitter-etch step	44
3-3 Process sequence for HBT from sidewall deposition to base metal deposition..	45
3-4 Process sequence for HBT from base mesa lithography to device passivation...	46
3-5 Schematic device structure after final metal deposition	48
3-6 SEM micrographs of HBT after different stages of the process.....	49
3-7 SEM micrographs of small-area HBT with emitter metal, base metal, collector metal and base mesa.....	50

3-8	Common-base (top) and common-emitter (bottom) I-V characteristics from large-area HBTs	51
3-9	Common-base I-V characteristics from small-area HBT	53
3-10	Ionization efficiency of Mg acceptors in GaN, and Fermi-level position for GaN doped with 10^{18} cm^{-3} Mg acceptors as a function of temperature	54
3-11	Temperature dependence of gain in large and small area HBTs	57
3-12	Layer Structure for the BJT with regrown emitter	58
3-13	TEM cross-section of BJT with regrown emitter	59
3-14	SEM micrographs of large area regrown emitter (top) and close-up of edge of regrown region (bottom)	60
3-15	SEM micrographs of small area regrown emitter in side view (top) and plan view (bottom)	61
3-16	Common-emitter I-V characteristics from small-area, regrown emitter BJT	62
4-1	HBT band diagram at $V_{CE}=10\text{V}$, $V_{BE}=4.2\text{V}$ (top) and current flow (bottom) for $\text{Al}_{0.2}\text{Ga}_{0.8}\text{N}$ emitter and base consisting of 5 pairs of $\text{Al}_{0.2}\text{Ga}_{0.8}\text{N}/\text{GaN}$ ($100\text{\AA}/100\text{\AA}$) doped at 10^{19} cm^{-3}	64
4-2	HBT band diagram at $V_{CE}=10\text{V}$, $V_{BE}=4.2\text{V}$ (top) and current flow (bottom) for $\text{Al}_{0.2}\text{Ga}_{0.8}\text{N}$ emitter and base consisting of 5 pairs of $\text{In}_{0.2}\text{Ga}_{0.8}\text{N}/\text{GaN}$ ($100\text{\AA}/100\text{\AA}$) doped at 10^{19} cm^{-3}	65
4-3	HBT band diagram at $V_{CE}=10\text{V}$, $V_{BE}=4.2\text{V}$ (top) and current flow (bottom) for $\text{Al}_{0.2}\text{Ga}_{0.8}\text{N}$ emitter and base consisting of 1 pairs of $\text{In}_{0.2}\text{Ga}_{0.8}\text{N}/\text{GaN}$ ($500\text{\AA}/500\text{\AA}$) doped at 10^{19} cm^{-3}	66
4-4	HBT dc current gain as a function of collector current for devices with AlGaIn emitter and different $\text{In}_x\text{Ga}_{1-x}\text{N}$ (5 pairs) base layers (top) or $\text{In}_{0.2}\text{Ga}_{0.8}\text{N}/\text{GaN}$ base layers of different numbers of pairs and different component layer thickness (bottom)	68
4-5	Effect of base doping on dc current gain (top), saturation current (center) or BV_{CEO} (bottom). The emitter doping was $1.8 \times 10^{19} \text{ cm}^{-3}$, collector doping $5 \times 10^{16} \text{ cm}^{-3}$ and base thickness 1000\AA in each case	70

4-6	Effect of emitter doping on dc current gain (top) and saturation current (bottom). The emitter doping was $1.8 \times 10^{19} \text{ cm}^{-3}$, collector doping $5 \times 10^{16} \text{ cm}^{-3}$ and base thickness 1000 Å in each case.....	72
4-7	Schematic of HBT structure used for the simulation and also the current flow Contours.....	76
4-8	HBT band diagram ($V_{CE} = 0$, $V_{BE} = 0$) for two different base doping levels, $5 \times 10^{17} \text{ cm}^{-3}$ (top) or 10^{19} cm^{-3} (bottom).....	77
4-9	Simulated common-emitter characteristics for HBTs with two different base doping levels, $5 \times 10^{17} \text{ cm}^{-3}$ (top) or 10^{19} cm^{-3} (bottom). The emitter doping was $1.8 \times 10^{19} \text{ cm}^{-3}$, collector doping $5 \times 10^{16} \text{ cm}^{-3}$ sub-collector doping 10^{20} cm^{-3} and base thickness in both cases.	78
4-10	dc current gain (top) and V_{CE} at the saturation point (bottom) as a function of base doping.....	79
4-11	BV_{CEO} (top) and saturation current (bottom) as a function of base doping for various collector doping levels	80
4-12	BV_{CEO} (top) as a function of collector doping (top) and Gummel plot (bottom) for a specific set of doping and thickness conditions.....	82
4-13	HBT gain versus collector current (top) and dc current gain and collector current versus emitter doping (bottom).....	83
4-14	DC current gain and collector current (top) and BV_{CEO} (bottom) as a function of thickness.....	85
4-15	Doping profile in GaN/InGaN HBT	87
4-16	Calculated band diagrams for HBT at $V_{CE}=0\text{V}$, $V_{BE}=0\text{V}$ (top) or $V_{CE}=15\text{V}$, $V_{BE}=4.2\text{V}$ (bottom)	89
4-17	Schematic of depletion region at operation condition for 1000 Å base, e-doping of $1.8 \times 10^{19} \text{ cm}^{-3}$ and c-doping of $5 \times 10^{16} \text{ cm}^{-3}$ at base doping of 10^{17} cm^{-3} (top) or 10^{18} cm^{-3} (bottom)	90
4-18	Gummel plots as a function of base doping (top) and dc current gain as a function of collector current (bottom).....	91
4-19	Common-emitter characteristics for base doping of either 10^{18} cm^{-3} (top) or $5 \times 10^{19} \text{ cm}^{-3}$ (bottom)	93
4-20	Early voltage (top) and BV_{CEO} (bottom) as a function of base doping.....	94

4-21	DC current gain (top), turning point of V_{CE} from saturation to active mode (center) and saturation current (bottom) base thickness (1000Å).....	95
4-22	V_{CEO} (top) and dc current gain (bottom) as a function of base thickness.....	96
4-23	BV_{CEO} (top) and dc current gain (bottom) as a function of emitter doping.....	98
4-24	Schematic of BJT structure.....	99
4-25	Current flow contours in GaN BJT at $V_{CE}=12V$, $V_{BE}=3.5V$	100
4-26	Gummel plots for 1000Å thickness base, 1.8µm width emitter mesa, 3µm wide base mesa, 4.2µm wide collector mesa with respective doping of $5 \times 10^{19} \text{cm}^{-3}$, 10^{19}cm^{-3} , $5 \times 10^{16} \text{cm}^{-3}$ for different materials	101
4-27	DC current gain as a function of collector current for the BJTs described in Figure 4.17.....	103
4-28	Common-emitter characteristics for GaN BJT with base doping of either $5 \times 10^{18} \text{cm}^{-3}$ (top) or $5 \times 10^{17} \text{cm}^{-3}$ (bottom).....	104
4-29	Saturated I_C (top) and BV_{CEO} (bottom) as a function of base doping for GaN BJT with 1000Å thick base, emitter doping $5 \times 10^{19} \text{cm}^{-3}$ and collector doping ($5 \times 10^{16} \text{cm}^{-3}$).....	105
4-30	BV_{CEO} as a function of either collector (top) or base (bottom) thickness. The base doping is $5 \times 10^{18} \text{cm}^{-3}$ emitter doping $5 \times 10^{19} \text{cm}^{-3}$ and collector doping $5 \times 10^{16} \text{cm}^{-3}$	108
4-31	f_T and dc current gain as a function of base (top) or collector (bottom) doping. The base is 1000Å thick in both cases	109
4-32	f_T versus base thickness (top) or base mesa size (bottom) for GaN BJT with emitter doping $5 \times 10^{19} \text{cm}^{-3}$, collector doping 10^{17}cm^{-3} , base doping 10^{19}cm^{-3} , emitter size 0.5µm and collector size 4.2µm	110
4-33	f_T versus emitter to base metal space (top) or emitter size (bottom) for GaN BJT with emitter doping 10^{19}cm^{-3} , base width 3µm and collector size 4.2µm.....	111
5-1	Schematic of simulated HBT structure	113
5-2	Common-emitter characteristics at 473 K (top) and 673 K (bottom) of GaN/InGaN HBT	115

5-3	Gummel plots at 300 K (top) and 700 K (bottom) of GaN/InGaN HBT with $V_{CE} = -12$ V	116
5-4	BV_{CEO} versus base doping (top) and temperature (bottom) at a collector current of $-1\mu A$. In the former case both completely ionized and partially ionized acceptors in the structure are shown. The emitter doping was 10^{19} cm^{-3}	117
5-5	I_C or a function of temperature for $V_{CE} = -20$ V and $I_B = -5$ or $-50 \mu A$	118
5-6	I_C , I_B and gain as a function of temperature for $V_{CE} = -12$ V, $V_{BE} = -3.5$ V, emitter doping of $5 \times 10^{19} \text{ cm}^{-3}$ and base thickness 1000 \AA	119
5-7	f_T versus temperature for emitter doping $5 \times 10^{19} \text{ cm}^{-3}$, $V_{CE} = -40$ V or -12 V	121

Abstract of Dissertation Presented to the Graduate School
of the University of Florida in Partial Fulfillment of the
Requirements for the Degree of Doctor of Philosophy

DESIGN AND FABRICATION OF GaN-BASED HETEROJUNCTION BIPOLAR
TRANSISTORS

By

Kyu-Pil Lee

December 2003

Chairman: Stephen J. Pearton

Major Department: Materials Science and Engineering

A self-aligned fabrication process for small and large emitter contact area ($2 \times 4 \mu\text{m}^2$ and $1.96 \times 10^3 \mu\text{m}^2$ respectively) GaN-based heterojunction bipolar transistor and bipolar junction transistors is proposed. The process features dielectric-spacer sidewalls, low-damage dry etching and selected-area regrowth of GaAs(C) on the base contact, and self-aligned emitter base regrowth processes are provided. The junction current-voltage (I-V) characteristics were evaluated at various stages of the process sequence and provided an excellent diagnostic for monitoring the effect of plasma processes such as CVD or etching. A comparison is given with large emitter-area devices fabricated on the same material. The small-area devices are attractive for microwave power switching applications, provided that a high-yield process can be developed. Series resistance effects are still found to influence device performance.

In the dc performance of small and large emitter contact area GaN-based heterojunction bipolar transistors, the dc current gain of both types of device improves with temperature, which we ascribe to higher ionization efficiency of the Mg acceptor in the p-base region. The presence of a resistive base layer at room temperature forces base current to flow directly to the collector, reducing the current gain.

However, to date, all of the reported GaN-based heterojunction bipolar transistors (HBTs) and bipolar junction transistors (BJTs) have had lots of problems to be solved even if there are many advantages to this technology. To predict the performance of GaN-based HBTs and BJTs, we simulated these structures with 2-dimensional device simulators.

The effects of base doping and thickness on dc current gain, collector-emitter saturation voltage, saturation current, collector-emitter breakdown voltage, rf characteristics (f_T) and the effects of impurity ionization as a function of device operation temperature of GaN, AlGaN, InGaN-based heterojunction bipolar transistors, and junction bipolar transistors were investigated using a drift-diffusion transport model.

Different base layer designs (including superlattice bases) for GaN-based heterojunction bipolar transistors (HBTs) and BJTs were simulated with MEDICI code.

Given the low ionization efficiency of Mg acceptors in the base, it is important to design structures that avoid depletion of the base layer. The presence of a resistive base causes current to flow directly to the collector, severely reducing gain. The temperature effects of GaN-based heterojunction bipolar transistors were investigated by simulations. The contact resistances are all significantly decreased at high temperatures, where ionization efficiency is maximized.

CHAPTER 1 INTRODUCTION

The family of high-bandgap materials was a very promising class for making optoelectronic and electronic devices for the last 3 or 4 decades. One group of high-bandgap materials is III-V nitride materials. Wide-bandgap semiconductors offer the best technical promise for high-power and high-temperature transistors. Until recently, the most promising of these materials was silicon carbide (SiC). However, SiC has several technical shortfalls that have opened competition to the III-nitride materials. Thermal oxides in SiC power metal oxide semiconductor field effect transistors (MOSFETs) actually limit the temperature range of application since the gate contact degrades and becomes electrically leaky at high temperatures. The low electron mobility of only 400 $\text{cm}^2/\text{V.s}$ yields lower power added efficiency (PAE) ($<30\%$) for many transistors in the frequency range of 1 to 5 GHz. For silicon and SiC, amplifier efficiency decays rapidly with increase in frequency, so that it drops below 25% for many devices operating above 2 GHz. Finally, since SiC is a homogeneous material, the advantages of bandgap engineering (as seen in III-V compound electronic devices) are not available. One of the compound material devices (GaN-based device) offers wider bandgap, greater chemical inertness, and higher temperature stable operation than SiC.

Single-transistor output power is the most important cost-limiting issue for commercialization of solid-state power devices. Other economic factors relating to performance are PAE required for lightweight portable systems, amplifier linearity

necessary to transmit digital signals without distortion or out-of-band modulation products, and amplifier noise figure and phase noise. Output power achievable by microwave devices is directly proportional to the breakdown voltage and sustainable current limits. For bipolar devices under Class A operation, the maximum output power density is then

$$P_{\max} = \frac{1}{8} I_{\text{sat}} (V_{\text{BC}} - V_{\text{knee}})$$

where I_{sat} is the saturation current at the quiescent point, V_{BC} is the collector breakdown voltage, and V_{knee} is the saturation voltage at maximum current. Therefore, the output power capability of solid-state heterojunction bipolar transistors (HBTs) is then strongly influenced by the breakdown voltage resulting from design and fabrication of the collector epitaxial layers. Use of GaN in the HBT collector should yield tangible improvements in power performance based on a breakdown electric field of 50×10^5 V/cm compared to 0.3×10^5 , 0.4×10^5 and 25×10^5 V/cm for silicon, GaAs, and 6H-SiC, respectively. The GaN-based semiconductors also benefit from a very high sustainable electron-saturation velocity of 2.7×10^7 cm/s. This unique property, which has been shown to significantly benefit GaN field effect transistors (FETs), is the result of large energetic displacement between valleys in the conduction band profiles. Finally, higher breakdown voltage operation will yield a reduction of the critical base-collector capacitance and improvement in high frequency power bipolar performance, since power devices could be fabricated with smaller areas.

One of the most significant problems limiting single-transistor high-power devices is the heat dissipation required. Mature silicon radio frequency (RF) power

transistors are currently limited to about 125°C junction temperature (85-100°C ambient) with operation of little more than 1 W at 10 GHz. Due to leaky oxides, SiC does not increase this range enough to result in significant advantage. The GaAs technology has improved on this performance to yield 50 W at 10 GHz with state-of-the-art power FET technology. However, both silicon and GaAs devices suffer greater high temperature degradation than is expected from the wide bandgap GaN-based HBTs. The GaN devices can operate at 400°C or higher and should exhibit optimal performance somewhere near 250°C because of improved ionization of the carriers in the material.

Additional performance benefits could be attained with the application of HBTs (versus FETs) in 1-5 GHz microwave digital communication and range-finding systems. Overall microwave system performance is critically influenced by phase noise, a measure of the sideband noise spectral density offset from the carrier frequency. Digital transmitters are sensitive to the phase noise close to the carrier which degrades the adjacent channel interference and modulation into the intermediate frequency (IF) and degrades sensitivity and adjacent channel sensitivity. Phase noise therefore results in an increased bit-error-rate (BER) and channel spacing for digital microwave systems. Phase noise in microwave radar similarly affects image resolution and accuracy. Intrinsically high $1/f$ noise in field-effect transistor devices compared to bipolar transistors yields substantially higher phase noise characteristics; therefore, high electron mobility transistors (HEMTs) may have difficulty in meeting the requirements of some military power systems. Therefore, advances in high power wide bandgap HBT technology will result in significant gains in the economics and performance of military and commercial communication systems, radar, and sensing equipment.

Compared to that of HEMT devices, the progress in nitride based HBTs and bipolar junction transistors have been less dramatic. Although high power densities (with lower phase noise and better linearity) have been projected for HBTs, there have been major obstacles in attaining them.⁽¹⁻⁴⁰⁾ The main issues preventing the realization of high-performance III-N HBTs are 1) the p-type doping of the base region, 2) excessive emitter-collector leakage currents, 3) high recombination rate, and 4) reduced breakdown voltage at high temperature.

The last three problems are related to the high density of defects which are generally grown on mismatched substrate such as sapphire (Al_2O_3) or SiC. The most important reason for the first problem is that p-type conductivity is usually obtained by doping with magnesium (Mg) which forms a deep acceptor, with a ionization energy of about 0.15-0.2 eV, in GaN. Not listed above are problems encountered in the device processing of nitride HBTs. These include avoiding etching damage, reducing surface states, and obtaining low resistivity ohmic contacts.

Recent progress has been remarkable in the fabrication of nitride HBTs by a number of research groups.⁽¹⁻⁴⁵⁾ New processing and growth techniques have resulted in improved dc and rf operation of nitride HBTs. To address the problems associated with the large density of threading dislocations (TDs) in nitride films, growth on lateral epitaxially overgrown (LEO) GaN layers has been investigated. The density of TDs in low defect regions of LEO GaN wafers can be less than 10^6 cm^{-2} which is at least three orders of magnitude lower than the density of these defects in layers directly grown on sapphire. As a result, the magnitude of emitter-collector leakage in HBTs grown on LEO GaN layers was reduced by as much as 4 orders of magnitude.⁽⁴¹⁾ Our studies also showed

better overall dc performance for nitride HBTs that were grown on thicker GaN buffers prepared by MOCVD. The density of dislocation in thick MOCVD grown layers is about 10 times less than those grown by molecular beam epitaxy (MBE).

To date, a great amount of work has been done to solve the problem of p-type doping in III-N films. This is a very important issue for both electronic and III-N devices. In addition to searching for optimum growth conditions for Mg-doping, different research groups have tried electron beam and high temperature annealing, co-doping with Mg-Si and Mg-O, and using p-doped AlGaIn/GaN superlattices (which we will call p-SL). So far, the p-SL proposed by Schubert et al.,⁽⁴⁶⁾ has been the most effective. In this technique when only the barrier (AlGaIn) layers were doped with a high density of Mg ($\sim 10^{19} \text{ cm}^{-3}$), both acceptor ionization efficiency (i.e., hole concentration) and carrier mobility were increased such that the conductivity increased by an order of magnitude compared to bulk Mg-doped GaN. The main reason for this increased p-type conductivity is enhanced acceptor ionization by electron tunneling from wells to barriers in the p-SL. In fact, the Schubert research group⁽⁴⁶⁾ measured a Mg ionization energy of less than 60 meV in p-SL compared to an ionization energy of about 200 meV in bulk p-type GaN. As discussed before, such enhanced p-type conductivity would greatly improve the dc and rf performance of III-N bipolar devices. Unfortunately, this enhancement is limited to the in-plane component of the conductivity in p-SLs.⁽⁴⁷⁾ Hence, better ohmic contacts are realized, but vertical transport through the base (which is the important factor for HBT operation) is not improved. One of the most promising approaches is the use of a p-InGaIn or GaN/InGaIn superlattice base structure.^(42, 43) Excellent hole generation above 10^{19} cm^{-3} at room temperature has been reported in the latter case.⁽⁴³⁾

In this dissertation we describe a self-aligned fabrication process for these devices that includes dielectric sidewall spacers and selected-area growth of GaAs (C) on the base region to decrease p-type ohmic contact resistance and self-aligned process to reduce defects density for emitter- and base-regrowth GaN HBTs and BJTs are described together. Performance of the resulting device is compared with that of large-area devices fabricated as the same wafer.

We report simulations of GaN-based HBTs with a variety of different base layer structures including GaN-, $\text{Al}_x\text{Ga}_{1-x}\text{N}$ - and InGaN-based npn or pnp HBT and BJT devices. In this dissertation we use a drift-diffusion model to study the influence of device designs.

Chapter 2 presents the literature review related to GaN-based material characteristics and present, modeling and basic equations for device simulation. In Chapter 3, I discuss the fabrication of GaN-based HBT devices for high power high performance HBTs. Output results of npn GaN-based device simulation are discussed in Chapter 4, and temperature effects of the pnp GaN/InGaN HBT calculated with device simulator are given in Chapter 5. Chapter 6 summarizes the development of GaN-based HBTs.

CHAPTER 2 LITERATURE REVIEW

2.1 GaN-Based Material Characteristics

2.1.1 Physical Property

GaN-based semiconductors have attracted tremendous interest for their applications to blue laser and LEDs, high temperature, high power electronics, high density optical data storage, electronics for the aerospace and automobile industries, and telecommunication devices. Wide bandgap semiconductors in power amplifiers extend the radiation hardness of the circuit.⁽⁶⁾

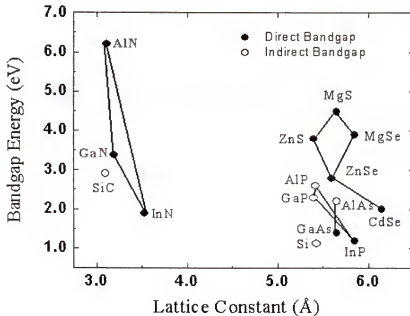


Fig. 2-1. The III-V compound semiconductor tree.

Reprinted with permission from <http://www.emf.co.uk/pages/utilities.htm>.

Fig.2-1 shows many of these compounds and their crystallographic lattice constant versus the energy band gap. Wide band gap electronic devices have excellent electrical and physical characteristics. Table 2-1 shows the physical parameters in different semiconductor materials. The most promising materials are GaN and SiC (band gap energy 3.4 eV and 3.2 eV respectively). For example, comparing the intrinsic carrier concentration at each different semiconductor material, 300 °C is needed to get $10^{15}/\text{cm}^3$ intrinsic carrier concentration (n_i) for Si materials, over 500°C is needed for GaAs. However, a much higher temperature is needed to get the same intrinsic carrier concentration in GaN, (about 1000°C). For these reasons, GaN related materials are much better for use in higher operation temperature compared to small bandgap materials such as Si or GaAs devices.

Table 2-1. Physical parameters in different semiconductor materials

	Si	GaAs	GaN	AlN	6H-SiC
Bandgap (eV) @300 °C	1.1	1.4	3.4	6.2	2.9
	Indirect	Direct	Direct	Direct	Indirect
Electron mobility ($\text{cm}^2/\text{V}\cdot\text{s}$), RT	1400	8500	1000 (bulk) 2000 (2D-gas)	135	600
Hole Mobility ($\text{cm}^2/\text{V}\cdot\text{s}$), RT	600	400	30	14	40
Saturation velocity ($\times 10^7 \text{ cm/s}$)	1	2	2.5	1.4	2
Breakdown field ($\times 10^6 \text{ V/cm}$)	0.3	0.4	>5		4
Thermal conductivity (W/cm)	1.5	0.5	1.5	2	5
Melting temperature (K)	1690	1510	>1700	3000	>2100

Gallium nitride (GaN) (shaped like small needles and platelets) was synthesized by Juza and Hann (1940). After that, many other research groups developed GaN related materials. Heterostructure electrical and optical devices were made by 20 years of development and refinement with various growth techniques such as molecular beam epitaxy (MBE), molecular organic chemical vapor deposition (MOCVD), and liquid phase epitaxy (LPE). The GaN was grown successfully on sapphire substrate in the late 1960s using chemical vapor deposition.⁽⁴⁸⁾ It became obvious that doping and defects would play a vital role in the future development of GaN.⁽¹¹⁾

The early unintentionally doped GaN was n-type, which at that time was thought to be due to nitrogen vacancies. The high n-type background carrier concentration (on the order of 10^{18} cm^{-3}) proved difficult to minimize; and the absence of a shallow acceptor dimmed the prospects of a production-scale GaN-based device effort.

Table 2-2. Ionization Energy of Impurities for Wurtzite GaN

Impurities	Ga-site (eV)	N- site (eV)	Remarks
Si	0.012-0.02		Donor
Native Defect (V_N)		0.03	Donor
C	0.11-0.14		Donor
Mg	0.14-0.21		Acceptor
Si		0.19	Acceptor
Zn	0.21-0.34		Acceptor
Native Defect (V_{Ga})	0.14		Acceptor
Hg	0.41		Acceptor

Reprinted with permission from M.E.Levinshtein, S.L.Rumyantsev, M.S.Shur, Properties of Advanced Semiconductor Material (Wiley Interscience, 2001).

Table 2-2 shows the ionization energy of impurities for GaN. Silicon is one of the most general n-type dopants for GaN since it effectively incorporates on the gallium site and forms a single shallow donor level. The Si is fully ionized at room temperature with an ionization level of ~ 30 meV.

The search for n- and p-type GaN was not successful until Amano et al.⁽⁴⁹⁾ demonstrated this feat in 1989. This remarkable achievement was actually a result of two significant milestones. First, the crystalline quality and the background n-type carrier density in unintentionally doped GaN films were significantly reduced by the use of a low temperature AlN buffer layer. A second p-type GaN was demonstrated with Mg-doping followed by an ex-situ low energy electron beam irradiation treatment. The ionization energy of Mg is 170 meV in the room temperature only under 10% of the total acceptors is ionized. Until now, one of the biggest obstacles to high performance using GaN related materials was high ohmic contact resistance and lateral high sheet resistance on the p-GaN substrate.

To get a low p-type ohmic contact resistance, high conducting p-GaN is needed. Even if the p-GaN substrate can always be heavily Mg-doped, several percent of dopants contribute to the conducting carriers due to the deep nature of the magnesium (Mg) level, which leads to incomplete acceptor ionization on the p-GaN substrate at room temperature. And high Mg the doping process may cause a Mg memory effect in the heterojunction structure. It is believed that because of the high Mg concentrations needed to adequately dope the p-type material, a substantial amount of Mg is left in an MOCVD reactor even after the flow is stopped. Figure 2-2 shows a large Mg tail past the point where the Si is turned on and the Mg is turned off.⁽¹¹⁾

Defects in the materials are a very critical factor in the effect to develop commercialized electronic power devices. HBT devices have complicated structures to flow the current vertically from emitter to collector. Defects in the GaN substrate especially affect HBTs characteristics and functions. As mentioned before, epitaxially grown GaN films basically have lots of dislocations caused by lattice mismatch between substrate and grown film (13% on sapphire, 3% on SiC substrate). Dislocations and point defects are a source of the leakage current at the emitter-collector junction or emitter-base junction in heterojunction bipolar transistors.

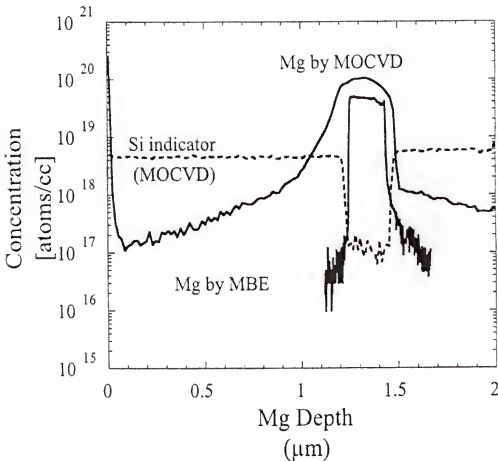


Fig. 2-2. SIMS profile of Mg tail in emitter of MOCVD grown npn structure compared with MBE grown junction.

(Reprinted with permission from IEEE Tran. Elec. Dev. 48 543 (2001).

In 1994, the lateral epitaxial overgrowth (LEO) technique was used to further improve the quality of the heteroepitaxially grown GaN, resulting in a marked reduction in defect density.⁽⁵⁰⁾ In this method, a layer of GaN grown by MOCVD is covered with 100-200 nm of amorphous silicon dioxide (SiO_2) and silicon nitride (Si_3N_4) with ex-situ techniques. Small circular or rectangular windows are then etched through to the underlying GaN. A GaN film is then regrown under conditions such that growth occurs epitaxially only in the windows and not on the mask. If growth continues, lateral growth over the mask eventually occurs. Since most of the extended dislocations propagate in the growth direction through GaN, very few threading dislocations (TDs) are visible in the regrown GaN that extends laterally over the mask. Using LEO growth methods, TDs can be reduced to 5 orders fewer defects than in a normally grown GaN. A refined approach to a nearly dislocation free GaN substrate for devices can be used by two successive LEO steps with the mask of the second step positioned over the opening defined by the mask of the first step.

In addition to growing GaN films with low defect densities, another key requirement for fabricating devices is the ability to precisely control the desired electrical properties of the thin film. In general, wide bandgap semiconductors are difficult to dope due to native defects. When the enthalpy for defect formation is lower than the band gap energy, the probability of generating a defect increases with the bandgap (i.e., the energy released by donor-to-acceptor transition).

In summary, to commercialize the GaN-based electronic devices, two critical limitations must be overcome: Increasing the p^+ substrate conductance; and reducing the defect density in GaN materials.

2.1.2 Transport Properties

The carrier mobility and saturation velocity in the semiconductor substrate are the primary determinants of the high speed transistor performance. The nature of the electron saturated velocity is reviewed next, followed by the electron mobility and its dependence of various scattering mechanisms.

2.1.2.1 Electron Saturation Velocity

The dependence of electron velocity on applied field and low field dependence of electron mobility for GaN were first calculated by Littlejohn et al. in 1976.⁽⁵¹⁾ They included electron scattering from acoustic phonons, polar optical phonons, ionized impurities and piezoelectric charge and predicted a peak in the electric drift velocity of 2×10^7 cm/s at a field of 10^5 V/cm. The work of Littlejohn et al. was further expanded by Gelmont et al.⁽⁵²⁾ to include the effect of upper valleys in the conduction band and account for intervalley scattering using a conduction valley separation of 1.5 eV. Gelmont predicted a peak electron velocity at 300K of 2.7×10^7 cm/s for an electron concentration of 10^7 cm⁻³ and a field of 150 kV/cm.⁽⁵²⁾

The peak electron velocity of InN has been calculated by O'Leary et al.⁽⁵³⁾ The calculated peak electron velocity is approximately two times the peak electron in GaN. However, the saturation velocity of InN was predicted to be equivalent to that of GaN or $\sim 2.5 \times 10^7$ cm/s. Therefore, InN-based transport layers will have increased frequency performance if ballistic transport can be achieved.

When considering the potential for ballistic transport and velocity overshoot effects in transistors it is important to know the distance over which such effects may occur. This has been calculated for GaN and InN for fields twice that for the peak

velocity.⁽⁵⁴⁾ At these fields significant velocity overshoot is expected to occur with InN calculated to achieve a peak velocity of 8×10^7 cm/s at a distance of ~ 0.1 μm .

2.1.2.2 Mobility Versus Impurities/Phonons

A very thorough theoretical treatment of the effect of ionized impurity scattering, polar optical scattering, piezoelectric scattering and acoustic scattering on electron transport in GaN and AlGaIn/GaN heterostructures is given by Shur et al.⁽⁵⁵⁾ Fig 2-3 shows the results of Shur for the electron mobility in bulk GaN as limited by polar optical, piezoelectric and acoustic scattering versus temperature. Polar optical scattering is seen to play a dominant role at temperatures greater than 200K due to the large optical phonon energy of GaN of 91.2 meV, while acoustic, and to lesser extent piezoelectric scattering dominates at lower temperatures.

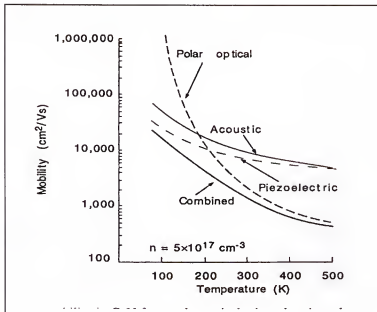


Fig. 2-3. Contributions to electron mobility in GaN from polar optical, piezoelectric and acoustics scattering, as a function of temperature.

(Reprinted with permission from M.S.Shur et al. Mater. Res. Bull. 22 (2) 44 (1997).

Figure 2-4 shows the calculated dependence of electron mobility versus temperature as limited by ionized impurity scattering for four electron and donor concentrations. It is clear that the mobility increases with electron densities which are due to increased screening of the impurities. This is particularly true for $n > N_T$ which approximates the situation in a 2DEG.

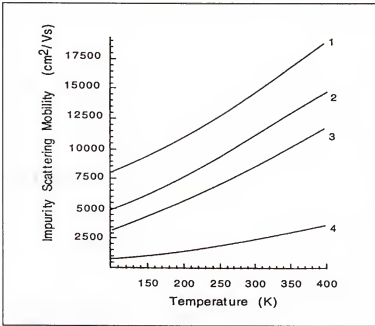


Fig. 2-4 Effect of ionized impurity scattering on electron mobility in GaN for total ionized impurity concentration of $7.5 \times 10^{16} \text{ cm}^{-3}$, and carrier densities of (1) $5 \times 10^{17} \text{ cm}^{-3}$; (2) $2 \times 10^{17} \text{ cm}^{-3}$; (3) $7.5 \times 10^{16} \text{ cm}^{-3}$; (4) $2 \times 10^{16} \text{ cm}^{-3}$.

(Reprinted with permission from B.E. Foutz et al. Proc. MRS 512 (1998) 555).

The combined effect of ionized impurity scattering, where mobility decreases with temperature, has been calculated.⁽⁵⁶⁾ Both the bulk case and 2DEG case are included in Fig. 2-5 for hexagonal and cubic GaN. At 300K, a 2DEG mobility near $2000 \text{ cm}^2/\text{Vs}$ was measured for a AlGaIn/GaN heterojunction structure grown on 6H-SiC with a sheet

electron density of $1.3 \times 10^{13} \text{ cm}^{-2}$.⁽⁵⁷⁾ At 10K the measured mobility increased to 10,250 cm^2/Vs .

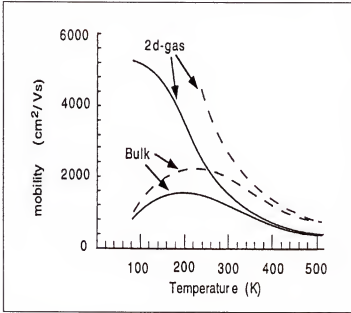


Fig. 2-5. Electron mobilities in cubic (dashed line) and hexagonal (solid line) GaN.
(Reprinted with permission from B.E. Foutz et al. Proc. MRS 512 (1998) 555).

2.1.2.3 Mobility Versus Dislocation

A model addressing the role of dislocations on electrons transport perpendicular to the dislocation has been developed by Weimann et al.⁽⁵⁸⁾ This is a critical consideration for GaN material grown on sapphire (a 12 % lattice mismatch) or SiC (3.5% lattice mismatch) since dislocation densities are typically between 5×10^{10} and $1 \times 10^{10} \text{ cm}^{-2}$. They assumed the GaN grew as hexagonal columns rotated relative to each other by a small angle, with dislocations propagating vertically between the columns. The dislocations were then treated as charged lines with the dependence of electron mobility calculated and measured experimentally. The increase of mobility with increased free electron

concentration with a maximum near 10^{18} cm^{-3} is due to increased screen of the charged dislocation core. This treatment suggests that transport in vertical devices (e.g., lasers, LEDs and HBTs) will be unaffected by the dislocations due to the repulsive band bending around the dislocations and the directional dependence of the scattering.⁽⁵⁸⁾

2.1.2.4 Minority Carrier Lifetime

Minority carrier lifetime is a critical parameter in the frequency response and detectivity of detectors, the gain of bipolar transistors, and the conductivity modulation of thyristors. Lifetime is also a critical measure of material quality as it relates to recombination centers. Several reports exist for measurement of recombination lifetimes in GaN with dislocation densities $> 1 \times 10^7 \text{ cm}^{-2}$. While the lifetime will depend on sample doping and surface quality (i.e., the surface recombination velocity), there are several reports on the minority hole diffusion length in n-type GaN giving values of 0.05 to 3.4 μm for n-type layers in range 1×10^{17} to $10 \times 10^{17} \text{ cm}^{-3}$ and dislocation densities in the $\sim 10^9 \text{ cm}^{-2}$.⁽⁵⁹⁾ This corresponds to a minority hole lifetime on the order of 1-20 ns. These values can be expected to improve as the dislocation density and point defect concentration are reduced.^(60, 61) In n-type material the electron diffusion length was 0.2 μm , with a lifetime of 0.1 ns.⁽⁶²⁾

2.1.3 Physical parameters of III-Nitride Semiconductors

Table 2-3 shows the physical parameters of III-nitride semiconductors.⁽⁶³⁻⁶⁶⁾ Group III-V semiconductors have excellent transport and optical properties, and they include a wide range of crystallographically lattice matched and strained compounds which enable the development of improved and new device structures through band gap engineering.

Table 2-3. Physical parameters of III-Nitride semiconductors

	Unit	GaN	AlN	InN
Crystal Structure		Wurtzite	Wurtzite	Wurtzite
Energy Gap	eV	3.39	6.2	1.9-2.05
Electron affinity	eV	4.1	0.6	
Number of atom	#/cm ³	8.9x10 ²²	9.58x10 ²²	6.4x10 ²²
Density	g/cm ³	6.15	3.23	6.81
Mobility (elec.) (hole)	cm ² /Vs	< 1000, 30, <200	135, 300 14	< 3200
Diffusion coeff. (elec) (hole)	cm ² /s	25 5	7 0.3	< 80
Density of state (C-band) (V-band)	/cm ³	2.3x10 ¹⁸ 4.6x10 ¹⁹	6.3x10 ¹⁸ 4.8x10 ²⁰	9x10 ¹⁷ 5.3x10 ¹⁹
Dielectric Constant (static) (dynamic)		8.9 5.35	8.5 4.6	15.3 8.4
Effective mass (elec.) hole (heavy) hole (light)	m ₀	0.2 1.4 0.3	0.4 3.53 3.53	0.11 1.69 0.27
Optical Phonon Energy	meV	91.2	99.2	89.0
Infrared refractive index		2.3	2.15	2.9
Piezoelectric Constant e ₁₅	C/m ²	-0.3	-0.48	
Piezoelectric Constant e ₃₁	C/m ²	-0.33	-0.58	-0.57
Piezoelectric Constant e ₃₃	C/m ²	0.65	1.55	0.97
Lattice Constant, a c	Å	3.189 5.186	3.11 4.98	3.53 5.69
Saturation velocity	cm/s	2.5 x 10 ⁷	1.4 x 10 ⁷	2.5 x 10 ⁷
Peak velocity	cm/s	3.1 x 10 ⁷	1.7 x 10 ⁷	4.3 x 10 ⁷

	Unit	GaN	AlN	InN
Peak velocity field	kV/cm	150	450	67
Breakdown field	V/cm	$\sim 5 \times 10^6$	$(1.2/1.8) \times 10^6$	
Specific heat	J/g °C	0.49	0.6	0.32
Thermal velocity (elec) (holes)	m/s	2.6×10^5 9.4×10^4	1.85×10^5 0.41×10^4	3.4×10^5 9.0×10^4
Debye temperature	K	600	1150	660
Thermal conductivity	W /cm·K	1.3	2.85	0.45
Melting Temperature	°C	2500	2750	650
Thermal diffusivity	cm ² /s	0.43	1.47	0.2

2.2 Simulation

In the semiconductor area, Computer Aided Design (CAD) is a very strong tool to develop devices and products in order to reduce time and cost. With CAD tools, device performances and characteristics can be predicted without actual device fabrications. There are three categories in the semiconductor simulation field.

The first category is the field of process simulation to set up the process technology. Using a process simulator, many of the semiconductor processes can be simulated to get physical and electrical characteristics in the devices, such as Chemical Vapor Deposition (CVD), sputtering, etching, ion implantation, photolithography, metallization, oxidation, thermal heat treatment, and process induced stress, etc.

SUPREM is one of the process simulator tools developed by Stanford University in 1977. Since then, the process models in SUPREM have developed substantially and will continue to evolve due to ongoing efforts.

The second category is for the device simulation. With device simulators, electrical dc and ac characteristics to evaluate devices performance, reliabilities can be predicted, as follows: current, capacitance, breakdown voltage, rf performance, electrical potential, etc. Several device simulators are explained more detail next.

The last category is related to the circuit simulator. It is a very powerful tool for circuit design and evaluation. With this tool, we can analyze electrical circuitry, for example, where errors occur, what points of design are weak, what performance devices show, how fast the devices can be operated, what operation margin the devices have, etc.

Simulation program for integrated circuits emphasis (SPICE) is one of the circuit simulators. It was developed at the University of California, Berkeley (1975). It is

important for integrated circuit simulation and SPICE is a possible tool to simulate circuit as temperature (default value 300K). SPICE can provide several types of circuit analyses as follows.

- Nonlinear DC and transient analysis
- Monte Carlo analysis
- Linear AC analysis
- Noise analysis
- Sensitivity analysis
- Distortion analysis
- Fourier analysis (frequency spectrum)

2.2.1 Device Simulators

Device simulators are strong tools to model the two-, or three-dimensional distributions of potential and carrier concentrations as well as current vectors in a device in order to predict its electrical characteristics for any bias condition. Simulators are useful not only for majority carrier devices involving a single carrier type, such as MOSFETs, JFETs, and MESFETs, but also for minority carrier devices involving both carriers (electrons and holes) such as p-n junction diodes, bipolar transistors, and p-n-p-n thyristors.

The accuracy of device simulation relies strongly on the input parameters and models used in the simulator. The simulation results are sensitive to the design of mesh points and grid formation methods, especially for non-planar device structures. The precise doping profile for small-geometry devices is not well defined, which makes the comparison between the simulation result and experimental data difficult. Further more, thermionic emission and tunneling mechanisms across the heterojunction were not modeled in many simulators until recently. Nevertheless, the device simulation provides a

relatively accurate model of device response with respect to boundary conditions. It also provides insight into devices operation and doping profile optimization.

The device simulators developed by industry and university include SEDAN (1984), BIPOLE (1993), BAMBI (Franz et al., 1989), MINIMOS (Fischer et al., 1994), PICES (1989), MEDICI (1993), DAVINCI (1993), ATLAS (1996), and FIELDY (Burtural et al. 1988). Table 2-4 shows the comparison of device simulators.

MEDICI is a two-dimensional (2-D) device simulation program that can be used to simulate the behavior of semiconductor devices such as bipolar junction transistors (BJTs), metal oxide semiconductor field effect transistors (MOSFET), heterojunction bipolar transistors (HBTs), optical devices etc. MEDICI is an enhanced version of PISCES. The MEDICI program allows all model and material parameters that are accessible to the user to be modified on a region-to-region basis. With its nonuniform triangular simulation grid, MEDICI can model arbitrary device geometries with planar and nonplanar surface topologies. MEDICI solves the semiconductor equations at each node within the devices. From the grid structure of the devices and impurity doping profile, MEDICI can provide two-dimensional contour and vectors.

2.2.1.1 MEDICI

It models two-dimensional distribution of potential and carrier concentrations in a device.⁽⁶⁷⁾ The program can be used to predict electrical characteristics for arbitrary bias conditions. The program solves Poisson's equation and continuity equations for both the electrons and holes to analyze devices. Medici simulates the behavior of deep submicron devices by proving the ability to solve the electron and hole energy balance equation self-consistently with the other device equations.

Table 2-4. Comparison of different device simulators

Simulator	Dimension	Model	Features	Remarks
POSES	1D	-	Schrödinger- Poisson solver	-
Leeds	quasi 2D	HD	Schrödinger equation	1D current equations
	-	-	Electrothermal model	Interfaces
<i>Fast Blaze</i>	quasi 2D	HD	-	1D current equations
	-	-	-	Interfaces
ATLAS	2D	DD,ET	TE heterojunction model	No tunneling
	-	-	-	Modeling
SIMBA	2D,3D	DD	Schrödinger equation	No ET (HD)
PISCES	2D	DD,ET	III-V models	-
G-PISCES	2D	DD	Full set III-V models	No ET(HD)
MEDICI	2D	DD,HD	Anisotropic properties	Mixed-mode
	-	-	-	Interfaces
MINIMOS-NT	2D	DD,HD	Full set III-V models	-
	-	-	TE/TFE model	-
DESSIS	2D,3D	DD,HD	Trap modeling, and TFE modeling	III-V modeling

Carrier heating and velocity overshoot are accounted for in MEDICI and their influence on device behavior can be analyzed. MEDICI uses a non-uniform triangular simulation grid and can model arbitrary device geometries with both planar and nonplanar surface topographies. The simulation grid can be also refined automatically during the solution process. Additional nodes and elements can be added where a user-specified quantity, such as potential or impurity concentration, varies by more than a specified tolerance over existing mesh elements.

This flexibility of the grids and mesh makes modeling of complicated devices and structures possible. A number of physical models are incorporated into the program for accurate simulations, including models for recombination, photogeneration, impact ionization, band-gap narrowing, band-to-band tunneling, mobility, and lifetime. MEDICI also incorporates both Boltzmann and Fermi-Dirac statistics, including the partial and complete ionization of impurities.

Advanced application modules are optionally available for MEDICI. They provide some unique and powerful capabilities for special purpose of applications. The presently available advanced application modules include heterojunction devices such as HBTs or HEMTs, optical devices, (charge coupled devices (CCDs), photodetectors and solar cells), anisotropic materials which show ability to account for the anisotropic behavior of semiconductor materials, trapped charge, (behavior of containing traps, such as thin film transistors (TFTs) and power devices), lattice temperature during device operation (lattice heating effects), circuit analysis, and programmable devices such as non-volatile memory devices (EPROMs, EEPROMs, and flash memories).

2.2.1.2 ATLAS

ATLAS provides a comprehensive set of physical models such as drift-diffusion transport models, energy balance transport models, and lattice heating and heatsinks. It is able to simulate graded and abrupt heterojunctions, hot carriers injections, band to band and Fowler-Nordheim tunneling, nonlocal impact ionization, thermionic currents, optoelectronic interactions, and stimulated emission and radiation. ATLAS has a modular architecture that includes other simulation tools such as MIXEDMODE, which offers circuit simulation capabilities that employ numerical physically based devices as well as compact analytical models, and INTERCONNECT3D, which provides capabilities for three dimensional parasitic extraction.

2.2.1.3 MINIMOS-NT

MINIMOS ⁽⁶⁸⁾ can perform Monte Carlo simulation of carrier transport. A Monte Carlo module couples self-consistently to the Poisson's equation and replaces the drift-diffusion approximation in critical devices areas. The model cards account for avalanche multiplication and hot carrier temperature effects.

It is a 2-dimensional device and circuit simulator consisting of a number of modules, such as the solver module, the mixed-mode module, the distributed device module, and the flow control. For the description, administration and storage of geometry, grid and attribute information the Profile Interchange Format (PIF) is used. The geometry, grid and attribute support modules support 2-dimensional access to data and offer a number of functions to deal with it, for example interpolation or grid refinement. The extension to three dimensions mainly affects these three key modules, where 3-dimensional structures must be introduced and the related functions must be extended.

The PIF is designed to specify 3-dimensional structures using points, lines, faces, solids, segments, and geometries, where additionally solid handling must be introduced to MINIMOS-NT.

MINIMOS-NT is capable of dealing with tensor product and triangular grids. For the representation of 3-dimensional structures tensor product and tetrahedral grids are commonly used. As a first step, tensor product grids will be implemented. For effective mixed-mode simulations, information about the dimensionality of a device must be hidden. Therefore, a convenient object-oriented design for the handling of devices has to be introduced. This encapsulation allows to use 1-, 2- and 3-dimensional devices within a circuit at the same time. In 3-dimensional simulations the equation system to be solved becomes very large. The computational costs increase dramatically. So performance is one of the main issues. Due to this fact, performance analyses over all modules are done to determine the critical ones.

2.2.1.4 PISCES-2ET

It is a dual energy transport version of PISCES-II. There are many new features available in the 2ET version, the capabilities to simulate the carrier and lattice temperatures and heterostructures in compound semiconductors. Various non-stationary phenomena such as hot carrier effects and velocity overshoot can be analyzed using PISCES-2ET. The electrical behavior of optoelectronic devices can be simulated with reasonable accuracy. Other new features that can be found in PISCES-2ET include as follow.⁽⁶⁹⁾

- High and zero frequency small signal AC analysis
- Improved initial guess using Newton projection method
- Carrier energy dependent mobility and impact ionization models

- About 10 different local and nonlocal field dependant mobility models
- Parameterization of array sizes for expansion of maximum grid number
- ASCII and binary exchange data format with process simulation programs

2.2.1.5 SEDAN

SEDAN (Semiconductor Device Analysis) is a computer program which performs the one-dimensional analysis of a semiconductor starting from the impurity profile (analytical or output of SUPREM) and solves for the electrical properties of the device.⁽⁷⁰⁾ These electrical properties can be completely described by five physical relationships: Poisson equation, electron and hole transport equations, electron and hole continuity equations. The recombination rate includes Shockley-Read-Hall and Auger recombination mechanisms. The transport equations have been written assuming the applicability of the Einstein relation for a non-degenerate semiconductor. A high impurity concentration effect, such as "band gap narrowing" is included. It consists of an effective forbidden gap narrowing due to overlapping of the electron wave functions associated with the impurity energy levels and the intrinsic conduction and valence band edges.

The integration is carried out by assuming the carrier mobility, the electric field intensity, and the current density to be constant between adjacent grid points. The time-dependent nature of the equations is accounted for by a time advancement method consisting of a quasi-linearization technique in which the two continuity equations are expressed in a truncated Taylor series.

The information obtained from the device analysis includes values of the dependent variables, as well as any parameters which can be derived from the dependent variables (such as quasi-Fermi levels, terminal currents, junction capacitances, integrated charge, etc.).

2.2.2. Basic Equations

The primary function of MEDICI is to solve the three partial differential equations (Eq. 2-1) self-consistently for the potential ψ and for the electron and hole concentration n and p , respectively. ^(67, 71)

$$\epsilon \nabla^2 \Psi = -q(p - n + N_D^+ - N_A^-) - \rho_s \text{----- (Poisson's equation)}$$

$$\frac{\partial n}{\partial t} = \frac{1}{q} \nabla J_n - U_n \text{----- (Continuity equations for electrons)}$$

$$\frac{\partial p}{\partial t} = -\left(\frac{1}{q}\right) \nabla J_p - U_p \text{----- (Continuity equations for holes) (Eq. 2-1)}$$

where ϵ and ψ are the permittivity and intrinsic Fermi potential respectively, N_D^+ and N_A^- are the ionized impurity concentrations, ρ_s is a surface charge density, that may be present due to fixed charge in insulating materials or charged interface states, U_n and U_p are the electron and hole recombination rates respectively.

From Boltzmann transport theory, J_n and J_p can be written as functions of the carrier concentrations and the quasi-Fermi potentials for electrons and holes (Eq. 2-2). Alternatively, J_n and J_p are able to be expressed as a function of ϕ , n , and p , consisting of drift and diffusion components

$$J_n = q\mu_n n \nabla \phi_n = q\mu_n n E_n + qD_n \nabla n \text{----- (Electrons current density)}$$

$$J_p = -q\mu_p p \nabla \phi_p = q\mu_p p E_p - qD_p \nabla p \text{---- (Holes current density) (Eq. 2-2)}$$

where, μ_n and μ_p are the electron and hole mobilities and D_n and D_p are the electron and hole diffusivities.

Although for most practical cases, full impurity ionization is assumed (i.e., $N_D^+ = N_D$ and $N_A^- = N_A$), the devices simulator also can model the incomplete ionization due to ionization energy of the impurities (Eq. 2-3)

$$N_D^+ = \frac{N_D}{[1 + g_c \exp(\frac{E_{Fn} - E_C + E_D}{kT})]}$$

$$N_A^- = \frac{N_D}{[1 + g_d \exp(\frac{E_V - E_{Fp} + E_A}{kT})]} \quad (\text{Eq. 2-3})$$

where g_c and g_d are the band degeneracy factor for electrons and holes respectively, E_{Fn} and E_{Fp} are the electrons and holes quasi-Fermi level, E_C and E_V are the conduction and valance band energy levels, E_D and E_A are donor and acceptor impurity activation energies respectively.

Currently Medici supports Shockley-Read-Hall, Auger, and direct recombination models (Eq. 2-4). Such as

$$U = U_n = U_p = U_{SRH} + U_{Auger} + U_{dir}$$

$$U_{SRH} = \frac{(pn - n_{ie}^2)}{\tau_n [n + n_{ie} \exp\{\frac{-(Et - Ei)}{kT}\}] + \tau_p [p + n_{ie} \exp\{\frac{-(Et - Ei)}{kT}\}]}$$

$$U_{Auger} = c_n (pn^2 - nn_{ie}^2) + cp(np^2 - pn_{ie}^2)$$

$$U_{dir} = d(np - n_{ie}^2) \quad (\text{Eq. 2-4})$$

where, E_i is the intrinsic energy, E_t is the trap density energy level, τ_n and τ_p are the electron and hole life times. c_n , c_p , and d are the constant dependent on the material.

For the isotropic element semiconductors, the bandgap and effective density of states in the conduction and valence band have temperature dependencies, as (Eq. 2-5)

$$n^2_i = N_c(T) \cdot N_v(T) \exp\left\{\frac{-E_g(T)}{kT}\right\}$$

$$N_c(T) = N_c(300) \cdot \left(\frac{T}{300}\right)^{\gamma_c}$$

$$N_v(T) = N_v(300) \cdot \left(\frac{T}{300}\right)^{\gamma_v}$$

$$E_g(T) = E_g(300) + \alpha \left\{ \frac{300^2}{(300 + \alpha)} - \frac{T^2}{(T + \beta)} \right\} \quad (\text{Eq. 2-5})$$

where n_i is the intrinsic carrier concentrations, E_g is the bandgap energy of the semiconductor, N_c and N_v are the density of states in the conduction and valence bands, α , β , γ_c , and γ_v are the constants depending on the materials. Note that ψ is related to the bandgap and the effective density of states by the expression (Eq. 2-6)

$$-q\psi = E_c - \frac{E_g}{2} - kT \ln \frac{N_c}{N_v} \quad (\text{Eq. 2-6})$$

2.3 GaN-Based Electronics Devices

From a technology perspective, we presently see a fairly even match between MOS, and bipolar technologies. High speed logic devices and central processing unit (CPU) devices continue to use bipolar transistors, while high density memories and large system chips are dominated by complementary-metal oxide semiconductor (C-MOS) devices composed of n-type and p-type MOSFETs. However, to get high speed and high

density devices, merged technology which is combined with bipolar transistors and C-MOS transistors was developed named BICMOS technology.

In addition, compound material technology has developed to the point where it is competing strongly with bipolar devices or Si-based C-MOS technologies for the high speed, high performance and high temperature operation.

2.3.1 Field Effect Transistors (FETs)

Technologies development of Si-based MOSFET and bipolar technology are amazing for 40 or 50 years. However there is a limitation to satisfy all of the new semiconductor technology with Si material for the electronic or optic devices.

To overcome the Si base technologies, III-N compound semiconductors have utilized a wide variety of structures to fabricate lateral field effect transistors (FETs), the most common being the metal semiconductor field effect transistors (MESFETs). This transistor utilizes a Schottky barrier surface potential to modulate the conductivity of a typically n-type channel near the semiconductor surface between the source and drain ohmic contacts. This structure was a modification to the basic junction field effect transistor proposed earlier (Shockley, 1952), which uses a reversed biased p-n junction formed between a p-type semiconductor gate region and the n-type semiconductor channel. The basic advantage offered by the MESFET was its simpler fabrication with a metal gate and a lower gate capacitance. Later attempts at metal insulator semiconductor field effect transistors in III-V semiconductors have been unsuccessful owing to the lack of a stable insulator with a low surface state density at the insulator to semiconductor interface, analogous to SiO_2/Si .

However recently, the development of thin film growth technologies such as MBE and MOCVD have given rise to advanced MOSFET structures beyond the MESFET. In heterostructure FETs known as HFETs, HIGFETs, or SISFETs, wider bandgap lattice matched semiconductors form the FET gate, which has a larger surface potential barrier than the MESFET. ⁽⁷²⁾

Another advantaged structure, which is rapidly gaining broad acceptance and utilization, is the high electron mobility transistor (HEMT), which utilizes a quantum well to create a two-dimensional electron gas (2DEG) channel free of ionized dopant atoms.

To realize high performance field effect transistors the following material and doping properties must be repeatably achieved.

- High resistivity buffer layers
- Controllable n-type doping between $\sim 1 \times 10^{17} \text{ cm}^{-3}$ (channel) and $> 1 \times 10^{19} \text{ cm}^{-3}$ (contact)
- Abrupt interfaces
- Modulation doping
- Low trap densities

Many electronic applications are involved with microwave frequency communications, such as wireless communications, satellite communications, etc.

2.3.1.1 Heterojunction Field Effect Transistors.

Heterojunction field effect transistors (HFETs) or high electron mobility transistors (HEMTs) are compound transistors. The heterojunctions are formed between semiconductors of different compositions and band gaps. This is in contrast to conventional MESFETs which utilize junction between homojunction materials. These

heterojunction devices offer advantages in microwave, high speed digital integrated circuits.

In heterojunction field effect transistors, the epitaxial layer structure is designed so that free electrons in the channel are typically separated from the ionized donors.

Heterojunction FETs have several advantages over conventional FETs because of the superior electron mobility and better electron confinement at the interface due to a larger conduction band discontinuity. The device current capability can be further improved by increasing in the center of the channel layer an additional planar doping. Fig. 2-6 shows the schematic HEMT structure.

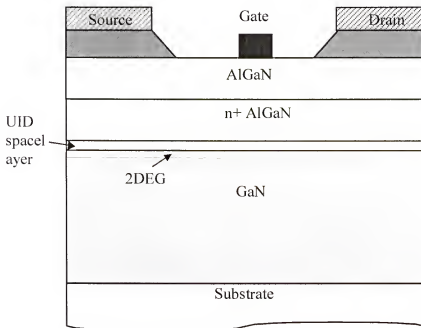


Fig. 2-6. Schematic structure of HEMT.

GaN-based HFETs are very attractive for power applications at high frequencies. This technology offers great potential for providing much higher output power, operational voltage and operating temperature for rf power amplifiers than is currently

possible with GaAs in the frequency range from X-band to Ka-bands. For the classifications of the frequency band, Table 2-5 describes the naming convention.

The other wide bandgap devices for these applications are SiC metal-semiconductor-field-effect transistors. However, for these devices the f_T and f_{MAX} values are typically in the 20GHz range and are, therefore, best suited for applications at frequencies below 7GHz. It appears likely that AlGaIn/GaN HFETs are better suited to higher frequency requirements due to the high electron mobility possible in heterostructures. These HFETs can also be grown on SiC substrates to exploit the high thermal conductivity of this material and have achieved excellent microwave, total power and power-added efficiency (PAE) results. For high power devices, it is necessary to employ multiple-finger type geometries.

Table 2-5. Naming conventions of the frequency bands.

Name	f_T	Name	f_T
	(GHz)		(GHz)
X	8-12	V	50-75
K	18-26.5	W	75-110
Ka	26.5-40	D	110-170
Q	33-50	G	140-220

AlGaIn HEMTs have made great progress for solid state power amplifiers with the demonstration of an X-band power density up to 9.8 W/mm. this high power density is the result of the high current and voltage capability of this materials system.

2.3.1.2 GaN-Based MOSFETs

A number of GaN FETs and AlGaIn/GaN HEMTs have been reported showing excellent device breakdown characteristics and power performance. However all show evidence of performance degradation due to the present of high parasitic resistances. The conventional low resistance n+ cap layer structure used to reduce parasitic resistances in GaAs technology is generally not applicable in nitride devices as it is difficult to perform the gate recess step. This is due to the high chemical stability of GaN that requires patterning by dry etching methods. However, dry etching of the gate recess open results in damage induced by ion bombardment, as observed by the corresponding low gate breakdown voltage. Moreover, it has been difficult to achieve stable Schottky contacts at high temperatures. The leakage currents through the Schottky contacts increase as the device temperature increases.

The promising problems regarding gate recess and devices stability at high temperatures can be over come by using GaN-based metal oxide semiconductor field effect transistors (MOSFETs) or metal insulator semiconductor field effect transistors (MISFETs) would provide for lower leakage currents and reduce power consumption. Another advantage of MOSFET is a large f_T over its MESFET counterpart, due to lower capacitance between source or substrate and gate. The most important requirement for having a GaN MOSFET or (MESFET) is to have an oxide or insulator deposited or grown on GaN, which gives a low interfacial density of state (D_{it}) high breakdown voltage of insulator film. As a consequence, the Fermi-level is not pinned at the insulator/GaN interface, and the charges can be accumulated or inverted, depending on the polarity of applied voltage. Fig. 2-7 shows the schematic structure of MOSFET.

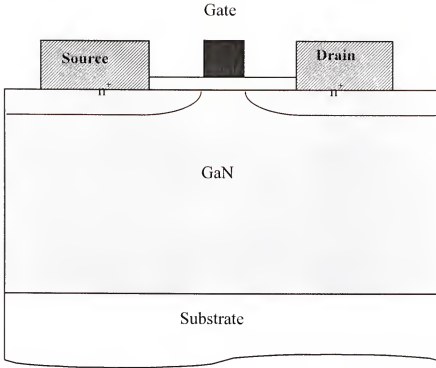


Fig. 2-7. Schematic structure of MOSFET

2.3.2 GaN-Based Bipolar Devices

Bipolar devices are particularly interesting for high current applications such as microwave power amplifiers for radar, satellite and communication in the 1-5 GHz range, powers >100 W and operating temperature > 425°C.

The concept of the heterojunction bipolar transistors (HBTs) was introduced by Williams Schokley in 1948, and the detailed theory of the devices was developed by Kroemer in 1957. The HBTs benefit from higher cutoff frequency, reduced base resistance, lower emitter-base and collector base junction capacitances, and higher Early voltage. In comparison with FET, heterojunction bipolar transistors have higher transconductance, higher current and power density, better threshold voltage, and lower $1/f$ noise.⁽⁷¹⁾

2.3.2.1 Physics of Heterojunction Bipolar Transistors

Figure 2-8 shows basic features of the energy band diagram for typical npn HBT biased in the active region of the common-emitter operation mode. In HBTs a wide bandgap material for emitter layer is used. The basic theory behind a wide bandgap emitter is as follows. Electrons ejected from the wide bandgap emitter into the base under emitter base forwarding bias condition. The electrons diffuse towards the collector and are caught up in the electric field of the reverse biased collector base junction, such as collector current. The other dc currents are hole current injected from the base into the emitter, and electrons-holes recombination currents due to electron-hole recombination in the emitter base space charge layer or in the p-doped base layer. Figure 2-9 shows schematically various current components in a HBT.

Table 2-6 shows the alignment of the conduction and valence bands at the emitter base heterojunction for different material combinations.⁽⁶³⁾ The conduction and valence bands at the emitter base heterojunction is such that a larger potential barrier is presented at the valence band than the conduction band. Especially the presence of spikes necessitates the inclusion of thermoionic emission and tunneling mechanisms for the carrier transport from emitter to base. The conduction band spike can be removed by using a compositional grading over the heterojunction and results in monotonically varying band edges (Grinberg et al. 1984). With the ability to control semiconductor bandgap variation, a gradual change in band gap across the base from bandgap (E_G) near the emitter to $E_G - \Delta E_G$ near the collector can be designed. This energy gradient constitutes a quasi-electric field that assists electrons across the base by drift. Electrons can be driven by these high quasi-electric field to velocities in excess of the value

predicted by steady-state velocity field curves. This results in a considerable improvement in base transit time and cut-off frequency.

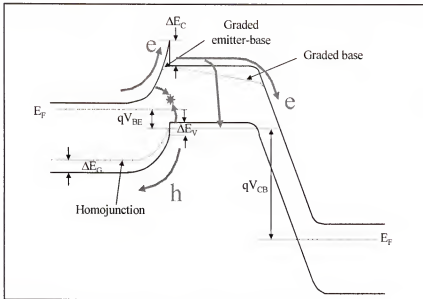


Fig. 2-8. Basic features of the energy band diagram of HBT

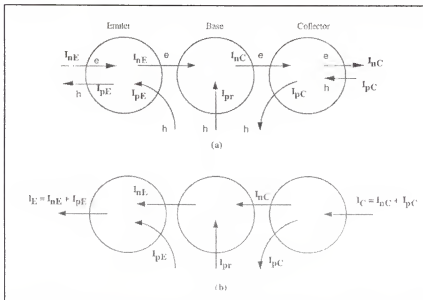


Fig. 2-9 Various current components in a HBT : (a) the arrow points to the direction of a carrier flow; (b) the arrow points to the direction of the current flow. (From; Williams Liu , Fundamentals of III-V Devices Wiley Inter-Science New York 1999).

Table 2-6. Band discontinuities at heterointerfaces

	ΔE_C (eV)	ΔE_B (eV)	Remarks
AlN/GaN	2.0	0.7	Wurtzite
InN/GaN	0.43	1.0	Wurtzite
GaAs/GaN		1.84	Cubic
InN/AlN	2.7	1.8	(0001)
SiC/AlN		1.4	(0001)

Reprinted with permission from M.E.Levinshtein, S.L.Rumyantsev, M.S.Shur, Properties of Advanced Semiconductor Material (Wiley Interscience, 2001)

Compared to a homojunction with similar doping densities, mobility and minority carrier lifetime, the ratio of hole flow to electron flow across the junction as equation 2-7.⁽⁷³⁾

$$\left(\frac{I_h}{I_e}\right)_{het} = \left(\frac{I_h}{I_e}\right)_{homo} \exp\left(\frac{-(\Delta E_g - \Delta E_C)}{kT}\right) \quad (\text{Eq. 2-7})$$

where the factor before the exponential term is the equivalent hole electron current ratio for a homojunction, ΔE_C and ΔE_g are the conduction band discontinuity (or spike) and bandgap difference across the junction, respectively, k is Boltzmann's constant and T is the absolute temperature. Since $\Delta E_C < \Delta E_g$ ($\Delta E_C \sim 0$ for a graded junction), the extra hole barrier can be extremely effective in limiting the hole current such that the emitter injection efficiency (the ratio of injected electron current to total junction current) is close to unity, regardless of the relative doping levels of the emitter and base. In addition, the

reduced hole injection cuts down minority charge storage in the neutral emitter, thereby improving the speed. Thus the HBT can be designed with regard to high frequency (highly doped base and low-doped emitter) without compromising the injection efficiency or gain). The limiting factor controlling the gain in high performance HBTs generally focuses on the electron hole recombination in the highly doped base. This is determined by the thickness and doping level of the base, both of which also affect the operating frequency of the device. The high base doping can increase the sheet conductance and reduce output conductance due to Early effect. A reduced emitter doping is possible in HBT devices, with consequent speed improvements as a result of the reduced emitter base depletion capacitance.

A double heterojunction bipolar transistor (DHBT) has two heterojunctions between emitter and base junction and base and collector junction. Valence band continuities exist in both the emitter and base, base and collector heterojunctions. Double heterojunctions have the beneficial effect of eliminating the injection of holes from the base into the collector when the base collector junction becomes forward biased. Increasing the collector bandgap reduces the charge storage in the collector and speeds up devices turn-off time from saturation. With DHBTs, symmetrical operation is possible such as upward and downward and can provide circuit design flexibility. Additional advantages of the wide bandgap collector are the increase in breakdown voltage and the reduction in leakage current.⁽⁷¹⁾

CHAPTER 3 PROCESS DEVELOPMENT FOR GaN-BASED BIPOLAR TRANSISTORS

3.1.Introduction

Heterojunction Bipolar Transistors (HBT) have a number of advantages over heterostructure field effect transistors (HFETs), including higher power density capability, better linearity, more uniform threshold voltages and higher transconductance. In the GaN/AlGaIn materials system there are several factors currently limiting the performance of HBTs ^(1-16,74,75) including the low p-type doping achieved in the base region of npn devices, the low electron lifetime in the neutral base, high leakage currents in the collector–emitter junction and high recombination rates. Some of these limitations may be alleviated with use of pnp structures, ^(17, 18) but the microwave performance of these would be expected to be inferior to npn devices.

While GaN/AlGaIn HBTs are attractive candidates for high frequency switching and communications applications, the main interest is in microwave power amplifiers in the 1-5 GHz frequency range and with operating temperature > 400 °C. To fulfill the frequency requirement, devices with small emitter-contact areas are necessary (i.e. < 10 μm^2). To date, all of the reported GaN/AlGaIn HBTs have had much larger active areas. ^(1-2, 4, 15, 18, 74) In this chapter we describe a self-aligned fabrication process for these devices that includes dielectric sidewall spacers and selected-area growth of GaAs (C) on the base region to decrease contact resistance. The resulting device performance is compared with large-area devices fabricated on the same wafer.

3.2. Process Development For Small-Area GaN-Based Bipolar Transistors

3.2.1 Experimental Methods

The layer structure was grown by metal-organic chemical vapor deposition (MOCVD) in c-plane sapphire substrates, as described previously.⁽⁵⁾ The structure consisted of a 2 μm undoped GaN buffer, a 1.44 μm thick n^+ ($3 \times 10^{18} \text{ cm}^{-3}$) GaN sub-collector, a 0.5 μm thick n ($3 \times 10^{16} \text{ cm}^{-3}$) GaN collector, a 0.15 μm thick p ($3 \times 10^{17} \text{ cm}^{-3}$) GaN base, a 0.1 μm thick n^+ ($n = 5 \times 10^{17} \text{ cm}^{-3}$) $\text{Al}_{0.15}\text{Ga}_{0.85}\text{N}$ emitter and a 500 Å grade to a 0.2 μm n^+ ($8 \times 10^{18} \text{ cm}^{-3}$) GaN contact layer.

All etching was performed in a Plasma Therm 790 series Inductively Coupled Plasma (ICP) system, using an ICP source power of 300 W (2MHz), a chuck power of 40 W (13.56 MHz), process pressure of 5 mTorr and gas mixture of $10\text{Cl}_2/5\text{Ar}$. The self-bias was -95 V under these conditions. Sidewall dielectric deposition was performed in a Plasma Therm system at 300 mTorr and 300 °C, using gas mixtures of $\text{SiH}_4/\text{N}_2\text{O}$ for SiO_2 and SiH_4/NH_3 for SiN_x . The emitter and collector metallization was $\text{Ti}(400\text{\AA})/\text{Al}(200\text{\AA})/\text{Pt}(300\text{\AA})/\text{Au}(3000\text{\AA})$, while the base metallization was $\text{Ti}(200\text{\AA})/\text{Pt}(250\text{\AA})/\text{Au}(1200\text{\AA})$, alloyed at 700° C 30 secs under N_2 . Figure 3-1 shows the layout of the small size mask set for this experiment. For the lift-off metallization process, masks have open space patterns.

3.2.2 Results And Discussion

3.2.2.1 Development of Self-Aligned Process

Figure 3-2 shows the process sequence for defining the emitter contact ($2 \times 4 \mu\text{m}^2$) using lift-off of AZ resist that was baked at 90 °C for 20 minutes. The sample was deep into toluene chemical bath for 20 minute after soft bake to get a fine lift-off metal pattern.




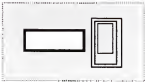

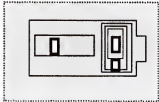
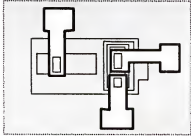
Step	Layout	Polarity
Emitter		Dark-field
Base-metal		Dark-field
Base-mesa		Clear-field
Collector-metal		Dark-field
Collector-mesa		Clear-field
Via-etch		Dark-field
Final-metal		Dark-field

Fig. 3-1. Mask layout of the small size HBT

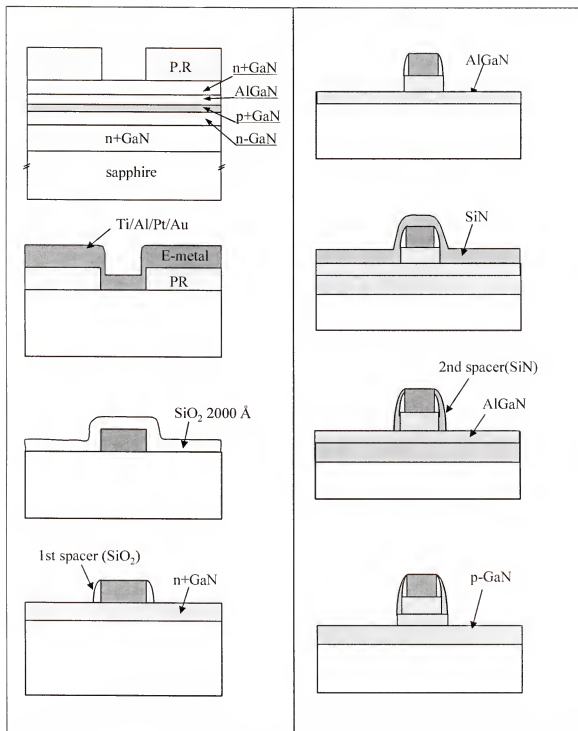


Fig. 3-2. Process sequence for HBT to the emitter-etch step

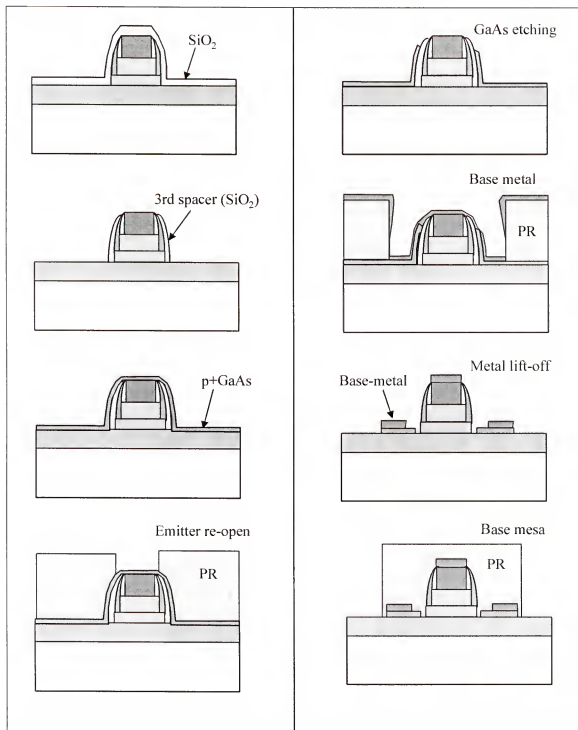


Fig. 3-3. Process sequence for HBT from sidewall deposition to base metal Deposition.

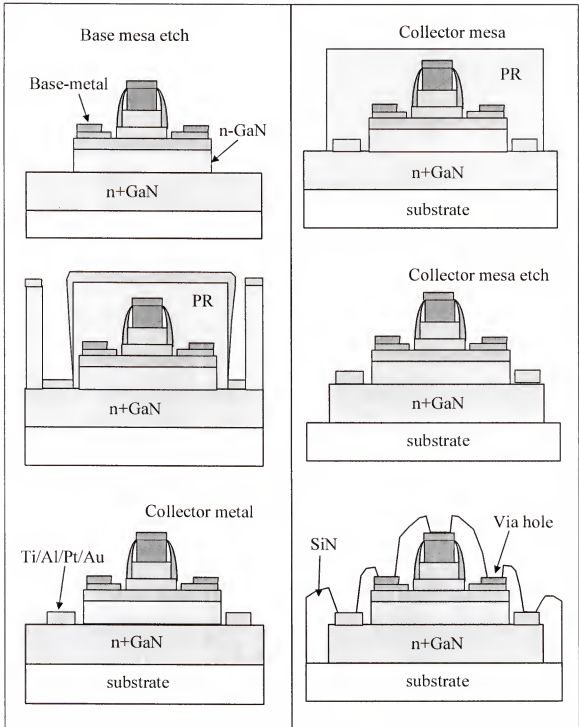


Fig.3-4. Process sequence for HBT from base mesa lithography to device passivation

Prior to metal deposition, the GaN surface was cleaned in HCl/H₂O for 1 min, followed by DI H₂O rinse and drying in filtered N₂. After deposition of 2000 Å of SiO₂, the sidewall spacer was formed by ICP dry etching of the field with SF₆ to expose the n⁺ GaN. Using the emitter contact as a self-aligned mask, the n⁺ GaN was dry etched down to the AlGaIn emitter. A SiN_x sidewall spacer was then formed by plasma enhanced chemical vapor deposition (PECVD) and subsequent dry etching of the field region using SF₆. The exposed AlGaIn emitter layer was removed by Cl₂/Ar dry etching down to the base layer, followed by wet (HCl) etching for 60 secs for clean-up of damaged GaN.

Figure 3-3 shows the process sequence down to the base metallization. First, a further sidewall spacer was formed by PECVD of 2000 Å of SiO₂, followed by lithography for the regrowth mask. The SiO₂ windows were opened by ICP SF₆ etching. MOCVD of 700 Å of p⁺ (10²⁰ cm⁻³) carbon-doped GaAs at 650 °C was followed by the emitter lithography and wet stripping of the poly-GaAs on the mask using 3 H₃PO₄/1 H₂O₂/50 H₂O at a rate of 850 Å·min⁻¹. After base metal lithography, the opening were descummed and rinsed for 60 secs in HCl/H₂O and then H₂O. The base metal was deposited and defined by resist lift-off.

Figure 3-4 (left) shows the fabrication sequence down to the collector metallization. After lithography, the exposed and base collector regions were removed down to the subcollector using ICP Cl₂/Ar dry etching. Following lithography, the collector contacts were deposited and defined by lift-off of the resist using a combination of soaking and spraying in acetone. The right handside of Figure 3-4 shows the final steps in the process, namely lithography for the collector mesa, deposition of a 2500 Å thick SiN_x passivation layer and opening of windows in the SiN_x using ICP SF₆ etching.

Figure 3-5 shows the schematic GaN/AlGaN HBT structure of the completed device using p+ GaAs regrowth film on p+ GaN base layer to reduce the base resistance and contact resistance. The final metal (200Å Ti/ 300Å Pt/ 3000Å Au) was patterned by lift-off.

Scanning Electron Micrographs (SEM) of the devices at various stages of the process are shown in Figure 3-6. At top left is a feature after emitter etching, while at top right is the feature after sidewall deposition prior to GaAs regrowth on the base. The SEM at bottom left shows a feature after collector mesa etching. These micrographs illustrate some of the problems with the process, namely that alignment needs to be very precise for these small-area devices, which is difficult given the topography and the fact

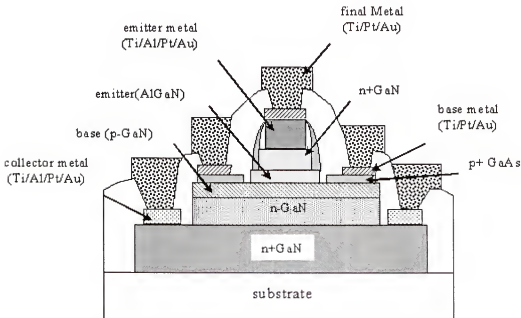


Fig. 3-5. Schematic device structure after final metal deposition

that lift-off is employed to define the metal contact. In addition, there is no dry etch selectivity between the AlGaIn emitter and underlying GaAs base and it is after difficult to remove the resist after high density plasma etching.

A Scanning Electron Micrograph (SEM) of the near-completed device was shown in Fig.3-7. The rough surface morphology is due to the high defect density in the epitaxial GaN on sapphire. The defects in the substrate affect working condition and reliability of the HBTs critically. The GaN surface morphology is also relatively rough compared to conventional homoepitaxial compound semiconductors employed for HBTs.

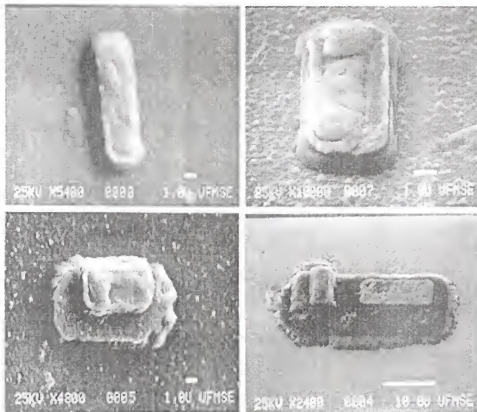


Fig. 3-6. SEM micrographs of HBT after different stages of the process

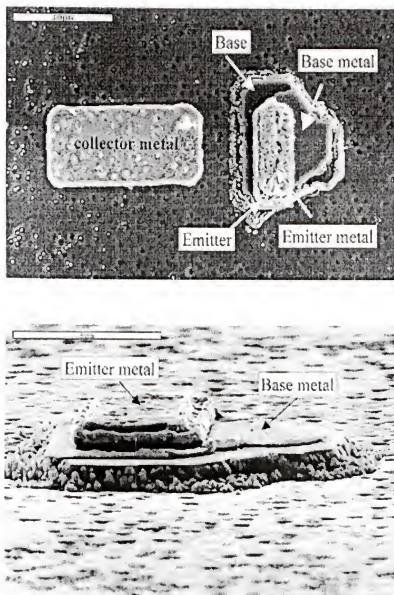


Fig. 3-7 SEM micrographs of small-area HBT with emitter metal, base metal, collector metal and base mesa.

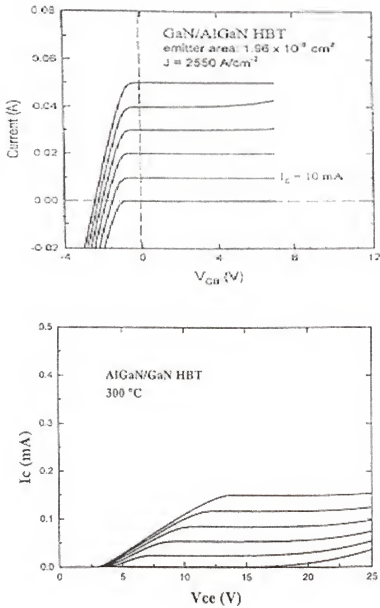


Fig. 3-8. Common-base (top) and common-emitter (bottom) I-V characteristics from large-area HBTs

The dc performance of large area ($1.96 \times 10^3 \mu\text{m}^2$ emitter) devices fabricated using the simple non-self-aligned process reported previously⁽⁴⁾ is shown in Figure 3-8. At top are the common-base characteristics measured at 25 °C. A maximum current density of $2.55 \text{ kA}\cdot\text{cm}^{-2}$ at 8 V was measured, corresponding to a power density of $20.4 \text{ KW}\cdot\text{cm}^{-2}$.

This measurement was limited by our test set-up and can be expected to improve with optimized devices and a true power mask-set. Note that $I_C \sim I_E$, indicating a high emitter injection efficiency. The offset voltage is in the range 2-3 V, similar to the built-in junction potential. The collector-base breakdown voltage, V_{BCB} , was $\geq 10 \text{ V}$, while the Early voltage was too large to measure accurately. Not all devices showed common-emitter characteristics, due most likely to the materials and processing problems mentioned earlier. The bottom of Figure 3-8 shows such characteristics obtained at a measurement temperature of 300 °C where the base resistance is decreased due to higher Mg acceptor ionization efficiency. These devices typically showed dc current gains of 2-5 at 25 °C and 10-15 at 300 °C.

On small-area devices we were only able to yet common-base characteristics, as shown in Figure 3-9. The current density was of the same order as for the large-area devices. We expect that further refinements in our process will significantly improve device performance.

In summary, a self-aligned process for small-area GaN/AlGaIn HBTs has been developed although there were many problems such as low breakdown voltage from emitter to collector and large leakage current. Further work is needed to optimize processes and improvements in material quality.

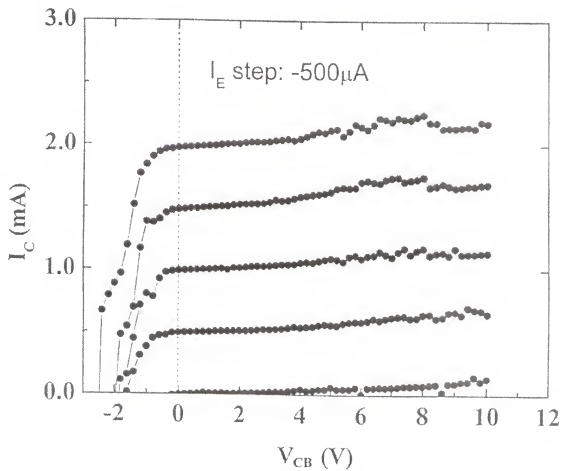


Fig. 3-9. Common-base I-V characteristics from small-area HBT

3.2.2.2 Temperature Dependent Performance of GaN-Based HBTs

From Fermi - Dirac statistics we can calculate the Fermi level position E_F for p-GaN containing 10^{18} acceptors $\cdot \text{cm}^{-3}$ as a function of absolute temperature T , from

$$N_A \frac{1}{1 + 2 \exp\left(\frac{E_a - E_F}{kT}\right)} = N_V \exp\left\{\frac{-(E_F - E_V)}{kT}\right\}$$

where N_A is the acceptor concentration, $E_a = 171$ meV for Mg in GaN and N_V is the valence band density of states. Using this relation, we calculated the ionization efficiency

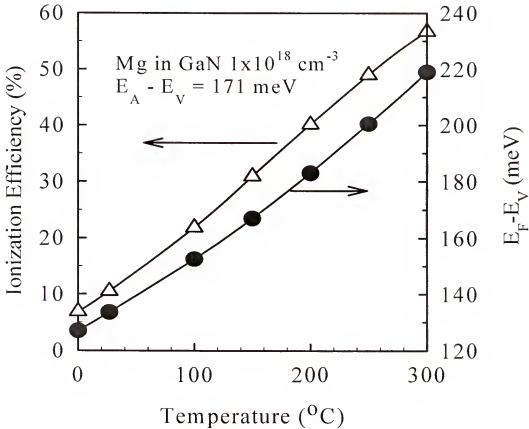


Fig. 3-10. Ionization efficiency of Mg acceptors in GaN, and Fermi-level position for GaN doped with 10^{18} cm^{-3} Mg acceptors as a function of temperature

for Mg as a function of sample temperature, as shown in Figure 3-10. At 25 °C, only ~10% of the Mg is ionized, whereas the efficiency increases to ~57% at 300 °C. Given the acceptor concentration in our films, this means the hole density rises from $\sim 10^{17}$ at 25 °C to $\sim 5.7 \times 10^{17} \text{ cm}^{-3}$ at 300 °C. Past investigations have shown a combination of thermionic emission and thermionic field emission as the dominant conduction mechanisms in contacts to p-GaN. At elevated operating temperatures, the hole density in the material increases rapidly, leading to a decrease in material sheet resistance. Concurrently there should be more efficient thermionic emission and tunneling of holes across the metal-GaN barrier, leading to a decrease in specific contact resistance and sheet resistance.

Table 3-1 shows the r_c values we have measured at 300 °C for several different p-contact metallizations on GaN. The substrate sheet resistance decreases with increasing temperature, indicating that the increased hole concentration plays a major role in decreasing r_c . Whilst device operation at elevated temperatures clearly would improve the p-contact resistance, it remains to be seen how much of a trade-off this entails in terms of degraded reliability. Figure 3-11 shows the measured dc current gain for both small and large area devices. When the Mg ionization efficiency is low (as at room temperature), a large portion of the base current flows directly to the collector and suppresses the current gain. As the base becomes more conducting at elevated measurement temperature, this effect is reduced and gain improves. Note that the large-area devices have significantly larger gains than the small emitter-area HBTs, which may be a result of surface

Table 3-1. Temperature-dependent contact data for p-GaN.

Contact	Measurement temperature (°C)	Specific contact resistance ($\Omega\text{-cm}^2$)	Contact resistivity ($\Omega\text{-mm}$)	Sheet resistance (Ω/\square)
Ni/Au	200	0.125	415.7	13900
Ni/Au	250	0.121	319.5	8470
Ni/Au	300	0.092	205.9	4600
W	300	0.682	758.4	

recombination of carriers. We are currently trying to optimize the deposition of H_2 -free dielectric passivation films on the HBTs.

In summary, the temperature dependent performance of large and small-area GaN/AlGaIn HBTs has been measured. The dc current gain is found to improve with temperature. These results are analyzed in terms of improved base resistance. A highly resistive base layer induced by the deep Mg nature forces base current flowing directly to the collector, bypassing the base. These carriers are usually required to control the amount of the base-emitter bias, and the amount of electron injection from the emitter to the base. Hence, reducing the free hole carrier concentration in the base has a direct impact on the current collected at the collector.

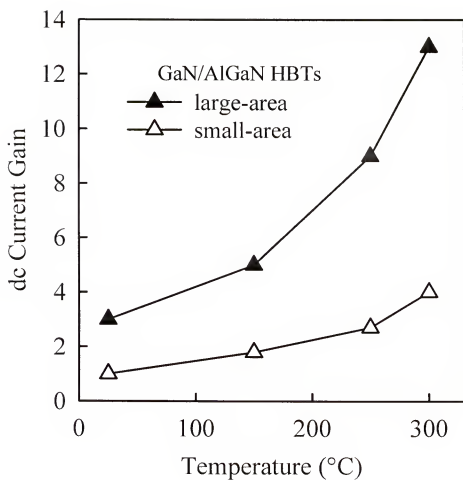


Fig. 3-11. Temperature dependence of gain in large and small area HBTs.

3.2.2.3. Emitter- And Base-Regrowth GaN-Based HBTs and BJTs

The layer structure for BJTs with p type-superlattice (p-SL) base and selectively regrown GaN emitters is shown in Figure 3-12. A similar process sequence was followed as for the HBTs, and n+-GaN selectively regrown through openings in a SiO₂ mask. A cross-sectional transmission electron micrograph of regrown GaN BJTs is shown in Figure 3-13.

We found that growth in relatively large open areas produced reasonable morphology and good edge acuity, as show in the SEM micrographs of Figure 3-14 for 70x70 μm^2 emitters.

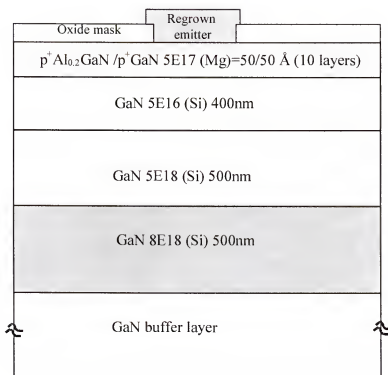


Fig. 3-12. Layer Structure for the p-SL with regrown emitter

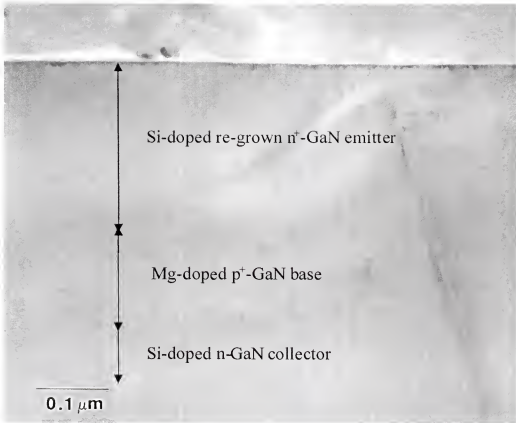


Fig. 3-13. TEM cross-section of BJT with regrown emitter.

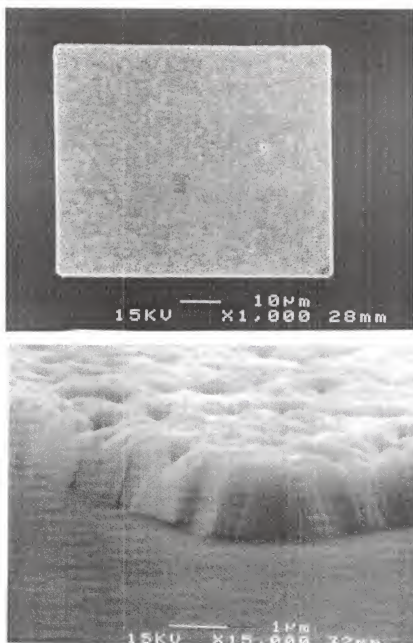


Fig. 3-14. SEM micrographs of large area regrown emitter (top) and close-up of edge of regrown region (bottom).

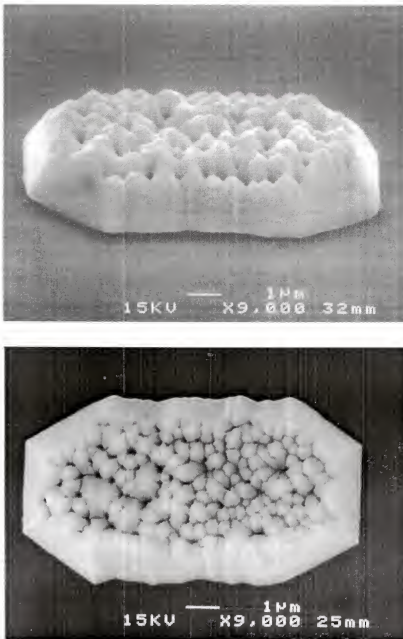


Fig. 3-15. SEM micrographs of small area regrown emitter in side view (top) and plan view (bottom).

The 3-dimensional surface of the growth was more obvious for small-area regrowth, as shown in Figure 3-15 which display a top and side view of the emitter area after removal of the SiO_2 mask. This may result from edge effects which influence the growth rate uniformity.

A room-temperature common-emitter characteristic from one of the small area devices is shown in Figure 3-16. The characteristic is clearly influenced by a high series resistance. In these devices the gain was < 5 at 25°C .

In summary, a self-aligned process for small-area GaN/AlGaIn HBTs and GaN BJTs with regrown base or emitter layers has been developed. Further work is needed on mask alignment, surface morphology, etch selectivity and device yield in addition to improvements in material quality.

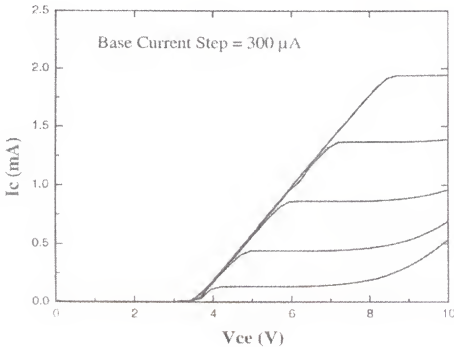


Fig. 3-16. Common-emitter I-V characteristics from small-area, regrown emitter BJT

CHAPTER 4 SIMULATION OF GaN-BASED NPN BIPOLAR TRANSISTORS

4.1. Introduction

In chapter 3, we report process and fabrication of the HBTs. There are two critical problems making HBTs with GaN-based materials. One is high p^+ ohmic contact on p^+ -GaN substrate, another is poor material quality by defects. Those problems limit getting high device performance and reliable characteristics. In this chapter we report simulations of GaN-based HBTs with a variety of different base layer structures including GaN/ $Al_{0.1}Ga_{0.9}N$ and InGaN/GaN superlattices of different periodicity and thickness. Only the InGaN/GaN structures are found to provide working devices. The effects of base and emitter doping in the dc performance of the HBTs are also examined.

4.2. Effects Of Base Structure On Performance Of GaN-Based Heterojunction Bipolar Transistors

4.2.1. Experimental Methods

The basic structure simulated consisted of a $0.5\mu m$ thick GaN sub-collector, $0.5\mu m$ thick GaN collector, a base structure of ; (i) GaN/ $Al_{0.1}Ga_{0.9}N$ with different numbers of pairs of these layers totaling $0.1\mu m$, (ii) $In_{0.2}Ga_{0.8}N$ /GaN with either $50\text{\AA}/50\text{\AA}$ (x10 pairs), $100\text{\AA}/100\text{\AA}$ (x5 pairs) or $500\text{\AA}/500\text{\AA}$ (1 pair) or (iii) $In_xGa_{1-x}N$ /GaN with graded x from 0 to 0.2 or 0.2 to 0. Finally, an emitter of either GaN or $Al_{0.2}Ga_{0.8}N$ was used. The MEDICI code employing the Heterojunction Device Advanced Application Module was employed, as discussed in detail previously. ⁽⁴⁵⁾

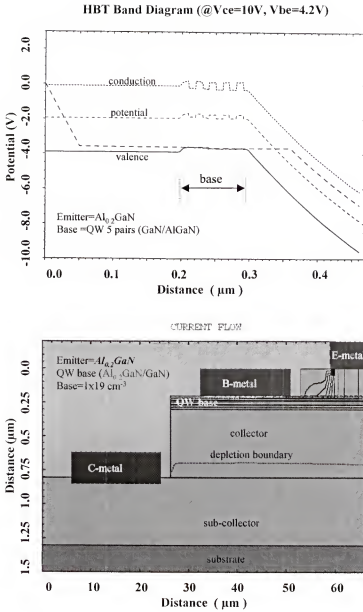


Fig. 4-1. HBT band diagram at $V_{CE} = 10V$, $V_{BE} = 4.2V$ (top) and current flow (bottom) for $Al_{0.2}Ga_{0.8}N$ emitter and base consisting of 5 pairs of $Al_{0.2}Ga_{0.8}N/GaN$ ($100A/100A$) doped at $10^{19} cm^{-3}$.

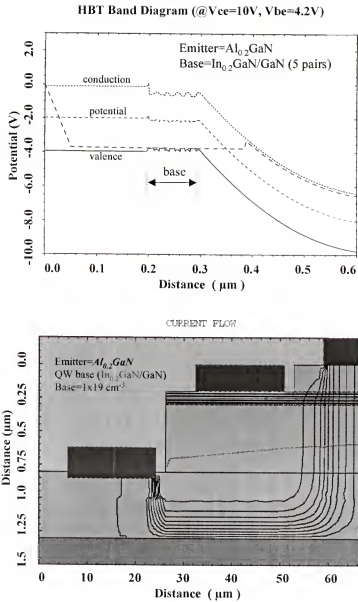


Fig. 4-2. HBT band diagram at $V_{CE} = 10V$, $V_{BE} = 4.2V$ (top) and current flow (bottom) for Al_{0.2}GaN emitter and base consisting of 5 pairs of In_{0.2}GaN_{0.8}/GaN (100Å/100Å) doped at 10^{19} cm^{-3}

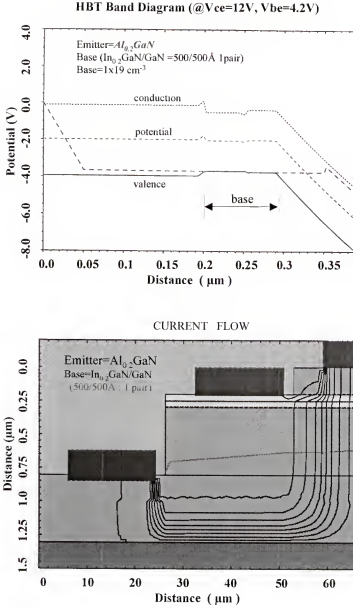


Fig.4-3. HBT band diagram at $V_{CE}=10\text{V}$, $V_{BE}=4.2\text{V}$ (top) and current flow (bottom) for $\text{Al}_{0.2}\text{Ga}_{0.8}\text{N}$ emitter and base consisting of 1 pairs of $\text{In}_{0.2}\text{Ga}_{0.8}\text{N}/\text{GaN}$ (500Å/500Å) doped at 10^{19} cm^{-3} .

4.2.2. Results And Discussion

Figure 4-1 (top) shows the HBT band diagram at $V_{CE}=10V$, $V_{BE}=4.2V$ for the structure with an $Al_{0.2}Ga_{0.8}N$ emitter and a base consisting of 5 pairs of $GaN/Al_{0.1}Ga_{0.9}N$ along with the simulated current flow for an effective base doping level of 10^{19} cm^{-3} (bottom). Note that we could not obtain active working devices for any of the $GaN/AlGaN$ base layer structures due to the barriers to current flow through the base.

By sharp contrast all the $InGaN/GaN$ base layer structures exhibited transistor characteristics. Figure 4-2 (top) shows the band diagram at $V_{CE}=10V$, $V_{BE}=4.2V$ for a structure with an $Al_{0.2}Ga_{0.8}N$ emitter and a base of $In_{0.2}Ga_{0.8}N/GaN$ (5pairs) with effective base doping again of 10^{19} cm^{-3} . The saturated current flow is shown at the bottom of Figure 4-2. Similarly, the band diagram and simulated current flow are shown in Figure 4-3 for a structure with an $Al_{0.2}Ga_{0.8}N$ emitter and the $500\text{\AA}/500\text{\AA}$ $In_{0.2}Ga_{0.8}N/GaN$ base layer with effective doping of 10^{19} cm^{-3} .

Table 4-1. Working condition of devices as process design

Base		Emitter	AlGaN	GaN
Q.W Base	GaN/AlGaN	All	X	X
	InGaN/GaN	50/50Å	O	O
	InGaN/GaN	100/100Å	O	O
Double	InGaN/GaN	500/500Å	O	O
Single	GaN or InGaN	1000Å	O	O

O : working, X: not working

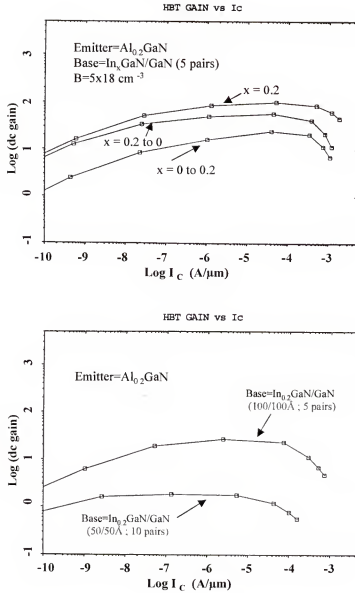


Fig. 4-4. HBT dc current gain as a function of collector current for devices with AlGaIn emitter and different $\text{In}_x\text{Ga}_{1-x}\text{N}$ (5 pairs) base layers (top) or $\text{In}_{0.2}\text{Ga}_{0.8}\text{N}$ / GaN base layers of different numbers of pairs and different component layer thickness (bottom).

Table 4-1 summarizes our initial study of all of the various base designs. Note that all variations of the GaN/AlGa_N superlattice base layer did not produce working HBTs, whereas all of the InGa_N/GaN base layer structures did show working devices.

Figure 4-4 (top) shows calculated dc current gains as a function of collector current for devices with graded In_xGa_{1-x}N/GaN (5pairs) base layer structures or with fixed In_{0.2}Ga_{0.8}N/GaN (5pairs) composition. There appears to be no advantage to the graded composition structures, which indicates that grading the bandgap to introduce a quasi electric field does not enhance the vertical transport through the base region by adding an electron drift component to the normal electron diffusion component. While, current gains depend on the activated total base concentration as indium ratio. There was little difference in gain for AlGa_N and Ga_N emitters in the case of the In_{0.2}Ga_{0.8}N/GaN (100Å/100Å, 5 pairs) base structure. In addition, Figure 4-4 (bottom) shows that 5 pairs produces a higher current gain than 10 pairs or 1 pairs (not shown). Table 4-2 shows the calculated main base current component for the different base structures. The electron component for base current is one of the dominant base current sources due to recombination of the confined electrons in base quantum well.

Table 4-2. Base current component for different base structures
(@ Ib=1μA, Vce=10V)

Base (InGa _N /Ga _N)	Emitter = Ga _N	Base main current components
Q.W Base (1x10 ¹⁹ cm ⁻³)	50/50Å	unknown
	100/100Å	elec. + hole
Double	500/500Å	elec. + hole
Single	1000Å	hole

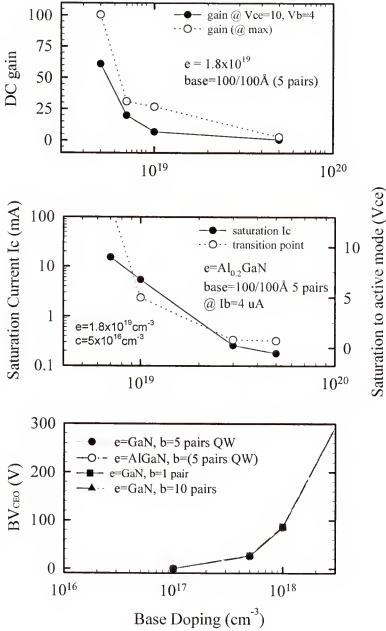


Fig. 4-5. Effect of base doping on dc current gain (top), saturation current (center) or BV_{CEO} (bottom). The emitter doping was $1.8 \times 10^{19} \text{ cm}^{-3}$, collector doping $5 \times 10^{16} \text{ cm}^{-3}$ and base thickness 1000 Å in each case.

Figure 4-5 shows the effect of base doping on various HBT performance parameters, including dc current gain (top), saturation current (center) and the breakdown voltage of the collector-emitter junction, BV_{CEO} (bottom). In the first two cases the results are for an $Al_{0.2}Ga_{0.8}N$ emitter doping of $1.8 \times 10^{19} \text{ cm}^{-3}$ and the 5 pairs $In_{0.2}Ga_{0.8}N/GaN$ base structure, while in the latter case the results are for either GaN or AlGaIn emitters and for different base structures. From this data, several conclusions can be drawn. Firstly, the base designs have little effect on BV_{CEO} . Secondly, saturation current falls off rapidly beyond a hole doping of $\sim 10^{19} \text{ cm}^{-3}$ as does dc current gain. In fact the maximum current gain falls below 10 for doping of a few 10^{19} cm^{-3} and devices of this type would be designed mostly for high-speed switching applications rather than power application.

Table 4-3 shows the collector current and ratio of electron to hole currents in the base of GaN emitter devices with different base layer designs. Once again it is seen that the decrease in gain at higher doping is at least partially the result of higher holes current increasing adding electron current component in base.

Table 4-3. Base current components as base doping

QW (100/100Å) 5 pairs (emitter=GaN)		I_c (mA) (@ $I_b=4\mu A$, $V_{ce}=10V$)	I (elec.)/ I (hole)
Base doping (cm^{-3})	7×10^{18}	12.3	3
	1×10^{19}	5.18	17
	3×10^{19}	0.26	58
	5×10^{19}	0.15	46

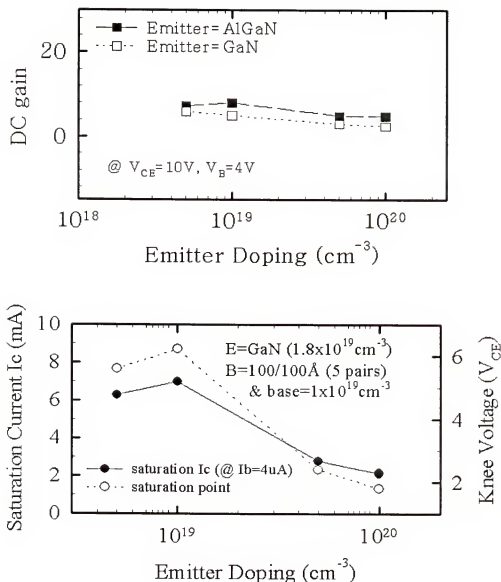


Fig. 4-6. Effect of emitter doping on dc current gain (top) and saturation current (bottom). The emitter doping was $1.8 \times 10^{19} \text{cm}^{-3}$, collector doping $5 \times 10^{16} \text{cm}^{-3}$ and base thickness 1000\AA in each case.

Figure 4-6 shows the effect of emitter doping on either dc current gain (top) or saturation current (bottom) for either GaN or AlGaN emitter (top) or only for GaN (bottom). The current gain has a relatively flat dependence on emitter doping and is higher for the AlGaN emitter due to the better carrier confinement, while saturation current peaks around a doping level of $\sim 10^{19} \text{ cm}^{-3}$. Table 4-4 shows the characteristics of the base current components as a function of emitter doping. The current is mainly due to electrons at high emitter doping levels.

Table 4-4. Base current components as a function of emitter doping

QW (100/100Å) 5 pairs (emitter=GaN)		Base current component (I _b)	Remarks I(elec.)/I(hole)
Emitter doping (cm ⁻³)	5×10^{18}	hole & <i>electron</i>	< 1
	1×10^{19}	hole & <i>electron</i>	~5
	5×10^{19}	<i>electron</i>	~ 100
	1×10^{20}	<i>electron</i>	> 400

Summary And Conclusions

The effects of base layer structure on the predicted performance of GaN HBTs was investigated using a drift-diffusion model. The use of AlGaN/GaN superlattices did not produce working devices for any of the conditions we employed. However InGaN/GaN superlattices, double or single layer bases all showed practical dc performance when employed in GaN HBTs. Grading of the InGaN composition was found to provide higher dc current gains than constant equivalent compositions in the

InGaN. Under these conditions, the choice of emitter materials (AlGaN or GaN) or emitter doping were not strong factors in influencing current gain.

4.3. Influence Of Layer Doping And Thickness On Predicted Performance Of npn AlGaIn/GaN HBTs

4.3.1 Experimental Methods

The basic layer structure employed was a 0.2 μm thick $\text{Al}_{0.2}\text{Ga}_{0.8}\text{N}$ emitter, GaN base of variable thickness, 0.5 μm thick GaN collector and 0.5 μm thick GaN sub-collector, with both the e-b and b-c junctions being abrupt. The dc characteristics were simulated using the MEDICI code, which is based on solving the Poisson and continuity equations of a 2D-structure, Physical models included Boltzmann transport theory, surface recombination, Shockley-Read-Hall recombination, Auger recombination and bandgap narrowing at high doping levels. A conduction band offset ratio Q_c of 0.7 was employed at the AlGaIn/GaN interface. The best currently available values of properties such as density of states, recombination coefficients, surface velocity, low field mobility and effective mass were employed.⁽⁷⁶⁾ Figure 4-7 shows a schematic of the HBT structure along with the current flow contours.

4.3.2 Results And Discussion

Figure 4-8 shows the unbiased ($V_{CE}=0$, $V_{BE}=0$) HBT band diagrams for two different base doping levels, $5 \times 10^{17} \text{ cm}^{-3}$ (top) and 10^{19} cm^{-3} (bottom), with fixed collector doping of $5 \times 10^{16} \text{ cm}^{-3}$ and emitter doping of $1.8 \times 10^{19} \text{ cm}^{-3}$. The potential barrier in valence or conduction band at the Figure 4-8 (top) is decreased about 0.8V by the low base doping concentration. The position of the Fermi level is also shows for both cases. Due to the large ionization level of Mg, the hole concentration in p-GaN is generally limited to $3\text{-}5 \times 10^{17} \text{ cm}^{-3}$ at room temperature, but at elevated temperatures the ionization efficiency increases and the hole concentration can approach the acceptor concentration of $\sim 10^{19} \text{ cm}^{-3}$.

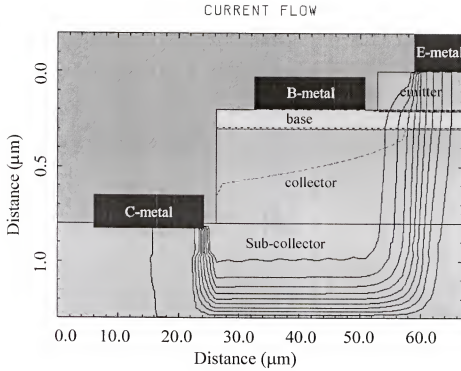


Fig. 4-7. Schematic of HBT structure used for the simulation and also the current flow contours.

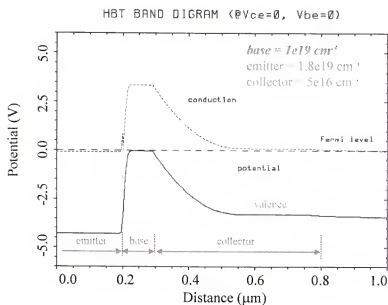
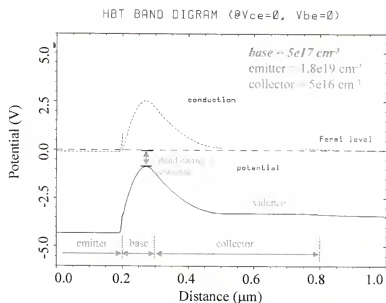


Fig. 4-8. HBT band diagram ($V_{CE} = 0$, $V_{BE} = 0$) for two different base doping levels, $5 \times 10^{17} \text{ cm}^{-3}$ (top) or 10^{19} cm^{-3} (bottom).

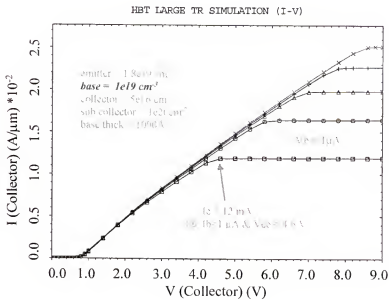
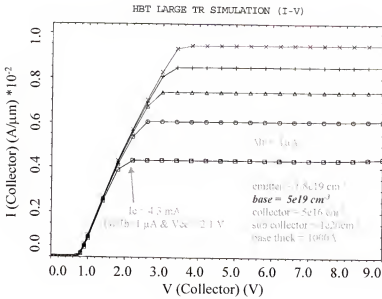


Fig. 4-9. Simulated common-emitter characteristics for HBTs with two different base doping levels, $5 \times 10^{19} \text{ cm}^{-3}$ (top) or 10^{19} cm^{-3} (bottom). The emitter doping was $1.8 \times 10^{19} \text{ cm}^{-3}$, collector doping $5 \times 10^{16} \text{ cm}^{-3}$, sub-collector doping 10^{20} cm^{-3} and base thickness in both cases.

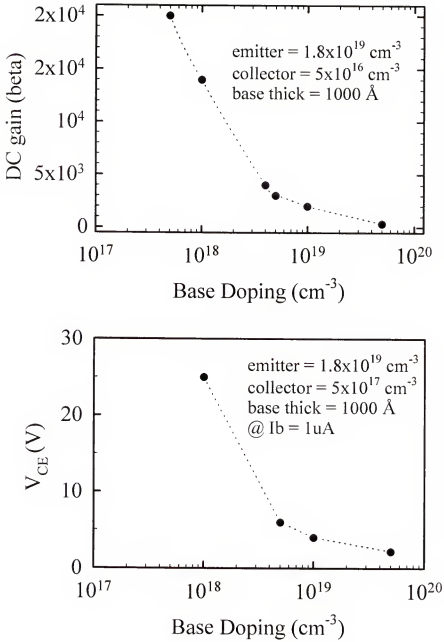


Fig. 4-10. dc current gain (top) and V_{CE} at the saturation point (bottom) as a function of base doping

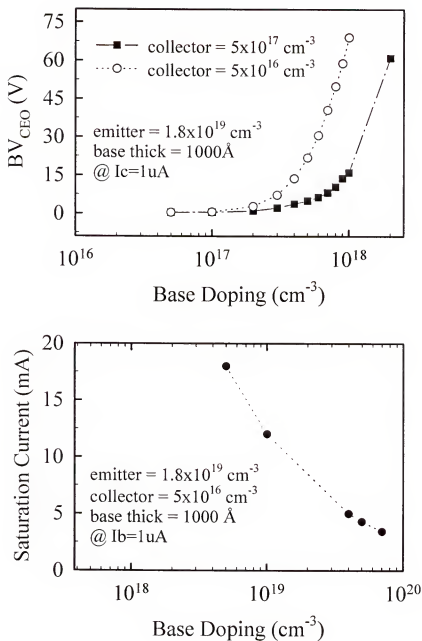


Fig. 4-11. BV_{CEO} (top) and saturation current (bottom) as a function of base doping for various collector doping levels

Figure 4-9 shows the common-emitter characteristics for two different base doping levels ($5 \times 10^{19} \text{ cm}^{-3}$, top and 10^{19} cm^{-3} , bottom) and a fixed base thickness of 1000 \AA . Note the effect of the higher base resistance on the slope of the I-V characteristics in the latter case. The saturated collector current was 4.3 mA at $I_b = 1 \mu\text{A}$ and $V_{CE} = 2.1 \text{ V}$ in the former case and 12 mA at $I_b = 1 \mu\text{A}$ and $V_{CE} = 4.6 \text{ V}$ in the latter case.

The effect of base doping on dc current gain and V_{CE} at the saturated current point are shown in Figure 4-10 for a fixed base thickness of 1000 \AA . Note that the gains can still be very high at a hole concentration in the base of 10^{19} cm^{-3} . The speed of the device can be traded-off in return for having larger values of both gain and V_{CE} at the current saturation point. Clearly, the experimental results from AlGaIn/GaN HBTs have not reached anywhere near this predicted performance due to the materials and processing problems discussed earlier, but the simulations to show the great promise of these devices for power amplification or switching at elevated temperatures where the Mg acceptors in the base are more fully ionized.

The influence of base doping on BV_{CEO} and saturated collector current are shown in Figure 4-11 for emitter doping of $1.8 \times 10^{19} \text{ cm}^{-3}$, a base thickness of 1000 \AA and two different collector doping levels. At this base thickness, the base is fully depleted at zero bias for low doping levels, leading to the unusual dependence of BV_{CEO} shown at the top of the figure. The effect of collector doping level on BV_{CEO} is shown in Figure 4-12 (top) for a fixed base doping of 10^{18} cm^{-3} , base thickness of 1000 \AA and emitter doping of $1.8 \times 10^{19} \text{ cm}^{-3}$. The junction breakdown voltage is still $>50 \text{ V}$ at this base doping level when the collector doping is $\sim 10^{17} \text{ cm}^{-3}$. Since much lower levels are achievable in clean MOCVD or MBE systems, it should be feasible to obtain breakdown voltages in excess

of 100V. A simulated Gummel plot is shown at the bottom of Figure 4-12 for a collector doping of $5 \times 10^{16} \text{ cm}^{-3}$, emitter doping $1.8 \times 10^{19} \text{ cm}^{-3}$ and 1000Å thick base doped at $5 \times 10^{19} \text{ cm}^{-3}$. The cross-over point for achieving gains above unity is close to that expected from the GaN bandgap.

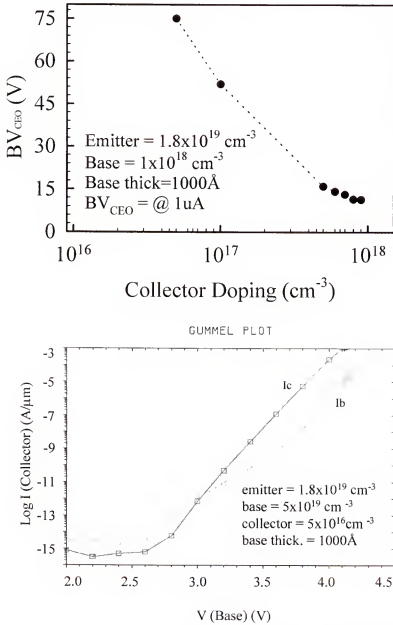


Fig. 4-12. BV_{CEO} (top) as a function of collector doping (top) and Gummel plot (bottom) for a specific set of doping and thickness conditions.

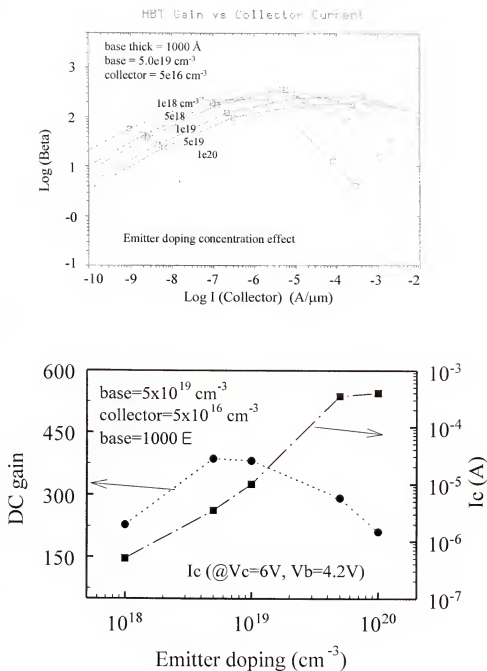


Fig. 4-13. HBT gain versus collector current (top) and dc current gain and collector current versus emitter doping (bottom).

Figure 4-13 (top) shows the HBT gain value collector current under similar conditions as a function of emitter doping concentration, while the bottom of the figure shows the maximum gain as a function of emitter doping and also the collector current at fixed biasing conditions ($V_C = 6V$, $V_B = 4.2V$). The maximum gain points shift to the higher collector current as increasing of emitter doping concentration, because the slope of the base current in ideal region of Gummel plot is decreased with increasing emitter doping concentration. In lower collector current condition, base current is affected by space charge recombination current at emitter base junction dominantly. However as increasing collector current, the effect of the base current component by the space charge recombination current decreases.

In HBTs, dc maximum gain (β_{max}) is in proportion to the emitter doping concentration and inversely to base doping concentration, however the difference of valence band offset voltage between emitter and base layers affects the dc gain exponentially. In this result, the gain goes through a maximum with emitter doping and is >400 at the peak.

Finally, Figure 4-14 shows the effects of base thickness on both dc gain, collector current (top) and BV_{CEO} (bottom). Collector current is directly proportional to the stored base charge and inversely proportional to base transit time generally. However the top of Figure 4-14 shows that collector current drops for a base thickness of 500\AA due to increased base sheet resistance. At a base doping of $5 \times 10^{17} \text{ cm}^{-3}$ (bottom), the base is fully depleted for thickness $< 1600\text{\AA}$. At higher base doping ($5 \times 10^{19} \text{ cm}^{-3}$, top) the current gain decreases with thickness due to the higher probability in recombination, but is still several hundred at a thickness of 1000\AA . This is consistent with past simulations. ^(9, 12)

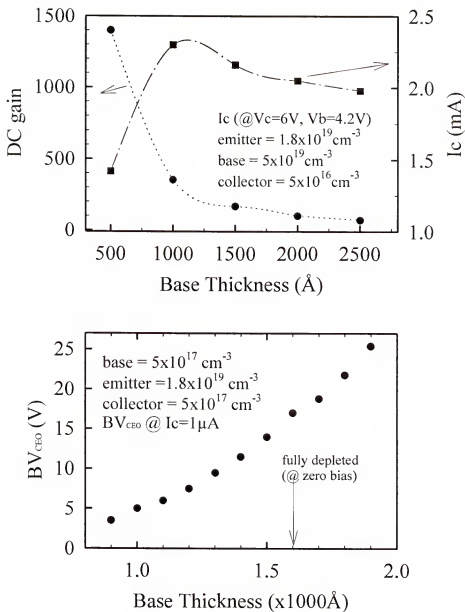


Fig. 4-14. dc current gain and collector current (top) and BV_{CEO} (bottom) as a function of thickness

In summary and conclusions, the low ionization efficiency of Mg acceptors in the GaN base, which controls the hole concentration and therefore the base resistance, is shown to have important effect on AlGaIn/GaN HBT performance through its influence in the base thickness needed to avoid depletion of this layers. Gains of several hundred are predicted at room temperature for practical doping levels.

4.4. Simulations Of InGaN-Base Heterojunction Bipolar Transistors

4.4.1. Experimental Methods

The basic structure used for most of the simulations was a sub-collector $0.5\mu\text{m}$ thick, collector $0.5\mu\text{m}$ thick, base of GaN/ $\text{In}_{0.2}\text{Ga}_{0.8}\text{N}$ $0.1\mu\text{m}$ thick (although this was varied in other cases) and $0.2\mu\text{m}$ thick GaN emitter. All of the junctions were assumed to be abrupt. The MEDICI code was used to simulate the dc characteristics, as a function of base doping and thick and also collector and emitter doping. The model includes field-dependent mobility, bandgap narrowing due to heavy doping, surface Auger recombination, Shockley-Read-Hall and also Boltzmann transport theory. A schematic of the doping profile is the standard structure as shown in Figure 4-15.

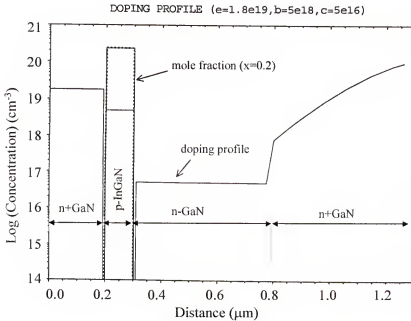


Fig. 4-15. Doping profile in GaN/InGaN HBT.

4.4.2 Results and Discussion

The unbiased ($V_{CE}=0$, $V_{BE}=0$) and biased ($V_{CE}=15\text{V}$, $V_{BE}=4.2\text{V}$) calculated band diagrams are shown in Figure 4-16 at fixed base doping (10^{18} cm^{-3}), collector diagram ($5\times 10^{16}\text{ cm}^{-3}$) and emitter diagram (10^{19} cm^{-3}), along with the position of the Fermi level. The biased result shows where flat-band conditions are achieved. Note that this is only achieved at reasonably large voltages in this wide bandgap materials system.

The depletion regions at the b-c junction are shown in Figure 4-17 for base doping of 10^{17} cm^{-3} (top) or 10^{18} cm^{-3} (bottom) for fixed base layer thickness of 1000 \AA , emitter doping of $1.8\times 10^{19}\text{ cm}^{-3}$ and collector doping of $5\times 10^{16}\text{ cm}^{-3}$. In base doping of $\geq 5\times 10^{18}\text{ cm}^{-3}$, the depletion layer extends parallel to the collector contact (i.e. reaches all the way to the sub-collector).

Simulated Gummel plots are shown in Figure 4-18 (top) as a function of base doping (5×10^{18} - $5\times 10^{19}\text{ cm}^{-3}$) for fixed emitter ($1.8\times 10^{19}\text{ cm}^{-3}$) and collector ($5\times 10^{16}\text{ cm}^{-3}$) doping. The Gummel plot is higher with base and collector storhed. The cross-over point for achieving above-unity gains is a base-emitter voltage of $\sim 3\text{V}$. The resultant dc current gains as a function of collector current are shown at the bottom of Figure 4-18. Maximum gains of $\sim 10^3$ (at a doping of $5\times 10^{18}\text{ cm}^{-3}$) and ~ 40 (at a doping of $5\times 10^{19}\text{ cm}^{-3}$) are achieved for the structure doping indicated wither the figure. Note that as the current is increased the relative effect of junction leakage is diminished and the intrinsic gains of the HBTs dominate. One advantage of use of InGaN in the base is the improved ohmic contact resistance that is possible relative to use of GaN (Mg) base layers. The gains would be degraded if poor quality ohmic contacts are present.

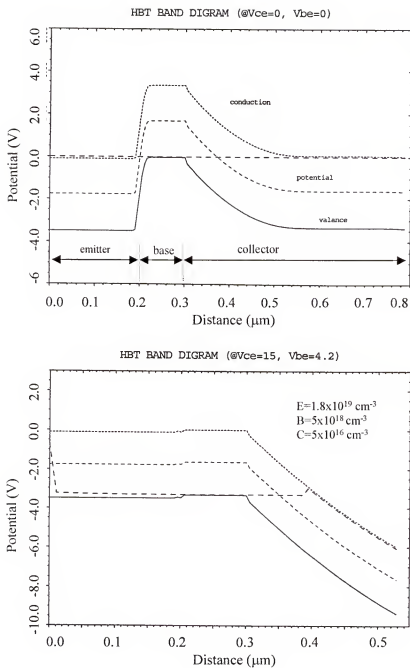


Fig. 4-16. Calculated band diagrams for HBT at $V_{CE}=0V$, $V_{BE}=0V$ (top) or $V_{CE}=15V$, $V_{BE}=4.2V$ (bottom).

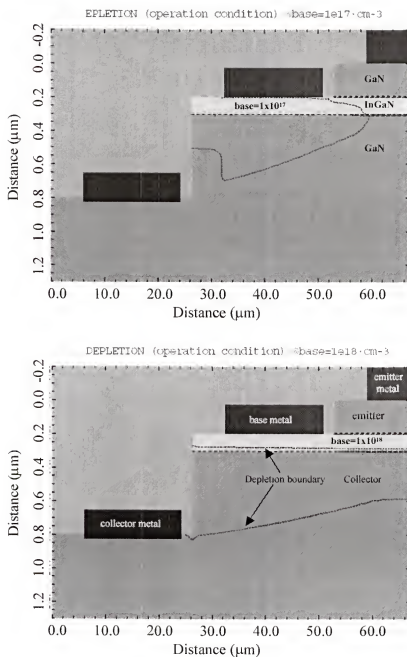


Fig. 4-17. Schematic of depletion region at operation condition for 1000 Å base, emitter doping of $1.8 \times 10^{19} \text{ cm}^{-3}$ and collector doping of $5 \times 10^{16} \text{ cm}^{-3}$ at base doping of 10^{17} cm^{-3} (top) or 10^{18} cm^{-3} (bottom).

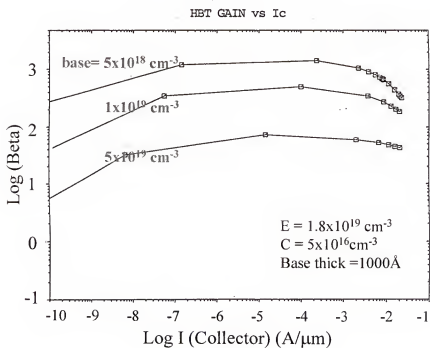
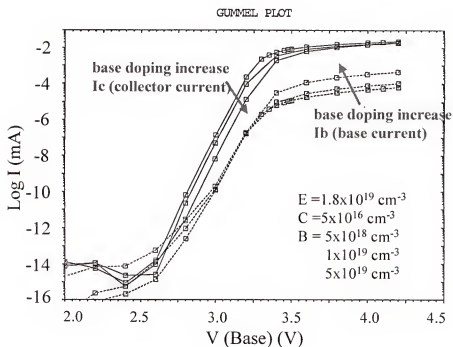


Fig. 4-18. Gummel plots as a function of base doping (top) and dc current gain as a function of collector current (bottom).

Simulated common-emitter characteristics for base doping of 10^{18} cm^{-3} (top) or $5 \times 10^{19} \text{ cm}^{-3}$ (bottom) are shown in Figure 4-19 for emitter doping of $1.8 \times 10^{19} \text{ cm}^{-3}$ and collector doping of $5 \times 10^{16} \text{ cm}^{-3}$. Saturation of the collector current is only achieved in the case of the higher base doping. Quite reasonable common-emitter characteristics were obtained at a base doping of $5 \times 10^{18} \text{ cm}^{-3}$ and the InGaN base HBT shows a much reduced effect of series resistances compared to GaN base devices simulated under the same conditions.

The effect of base doping as the HBT Early voltage and BV_{CEO} are shown in Figure 4-20. The former ranges from ~ 10 to $\sim 400 \text{ V}$ over the base doping range of $10^{18} \text{ cm}^{-3} - 5 \times 10^{19} \text{ cm}^{-3}$, where the BV_{CEO} increases rapidly beyond the point where the base is not fully depleted at zero bias. This is a similar trend to the result obtained for GaN-base HBTs. At this stage there has not been a report of very detailed characteristics of InGaN base HBTs, so there is no experimental data with which we can compare our simulations.

Additional detail on the effect of base doping on gain and the turning point from saturation to active mode are shown in Figure 4-21. The data at top shows both the maximum gain and the gain at a V_{CE} of 15V and V_{BE} of 3.8V (i.e. the flat-band condition). The data at center shows that I_{C} does not reach saturation for base doping of $< 2 \times 10^{18} \text{ cm}^{-3}$. The V_{CE} at which the collector current is saturated for a base doping of $5 \times 10^{18} \text{ cm}^{-3}$ is $\sim 4 \text{ V}$. The saturation current is plotted at the bottom of the Figure for various base doping levels and is $\sim 8 \text{ mA}$ at a doping of $5 \times 10^{18} \text{ cm}^{-3}$.

The effect of base thickness on BV_{CEO} and dc gain is shown in Figure 4-22 for various base doping levels and fixed emitter and collector doping concentrations. At low base doping, BV_{CEO} is limited by depletion in that layer.

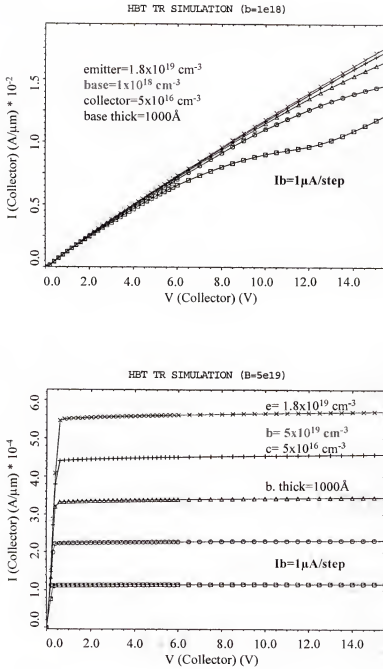


Fig. 4-19. Common-emitter characteristics for base doping of either 10^{18} cm^{-3} (top) or $5 \times 10^{19} \text{ cm}^{-3}$ (bottom).

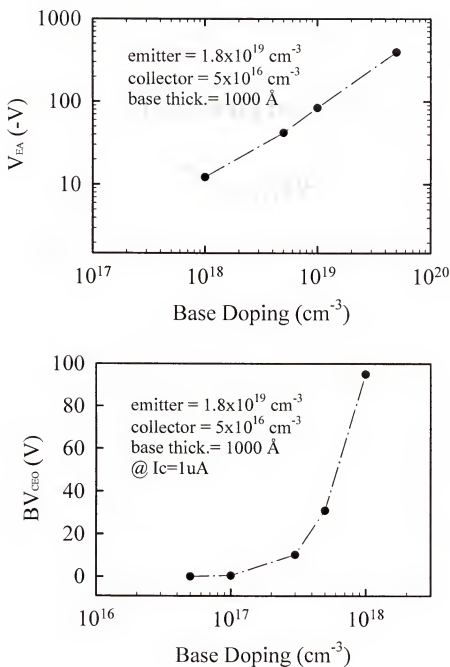


Fig. 4-20. Early voltage (top) and BV_{CEO} (bottom) as a function of base doping.

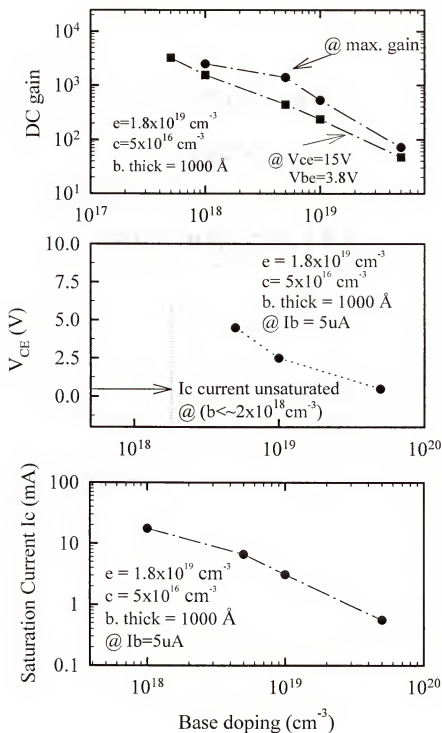


Fig. 4-21. DC current gain (top), turning point of V_{CE} from saturation to active mode (center) and saturation current (bottom) base thickness (1000Å).

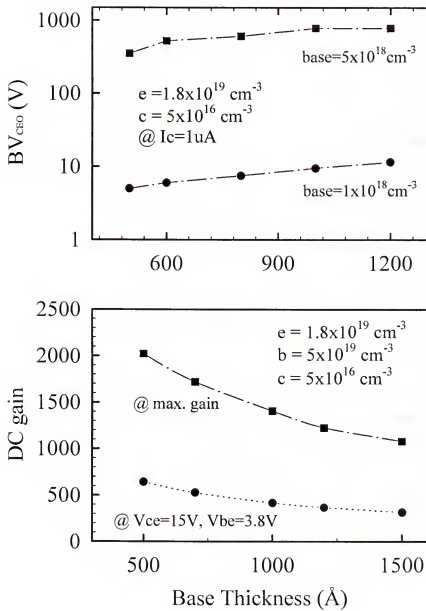


Fig. 4-22. V_{CEO} (top) and dc current gain (bottom) as a function of base thickness.

The bottom of Figure 4-22 shows the maximum calculated gain and the gain at flat band conditions ($V_{CE}=15$ V and $V_{BE}=3.8$ V). While the gain decreases with increasing thickness due to increased recombination, it remains at values of several hundred even for 1500 Å thick $\text{In}_{0.2}\text{Ga}_{0.8}\text{N}$ layers. The decrease in gain for the InGaN devices with increasing base thickness is less severe than for corresponding GaN base HBTs.⁽⁴⁵⁾

Finally, Figure 4-23 shows some effects of collector (top) or emitter (bottom) doping on BV_{CEO} (top) and dc current gain (bottom). Once again a base doping of at least $5 \times 10^{18} \text{ cm}^{-3}$ is desired in order to achieve a high BV_{CEO} , while high emitter doping is also a factor in achieving the largest dc current gain.

In summary and conclusions, the effects of layer doping and thickness on the predicted performance of GaN/ $\text{In}_{0.2}\text{Ga}_{0.8}\text{N}$ HBTs have been investigated using a drift-diffusion model. The InGaN base device is found to be attractive from a number of viewpoints including higher base conductivity and less sensitivity of gain on base thickness compared to AlGaN/GaN structures. It is still necessary to achieve good quality ohmic contacts and minimize junction leakage in order to have acceptable common-emitter characteristics.

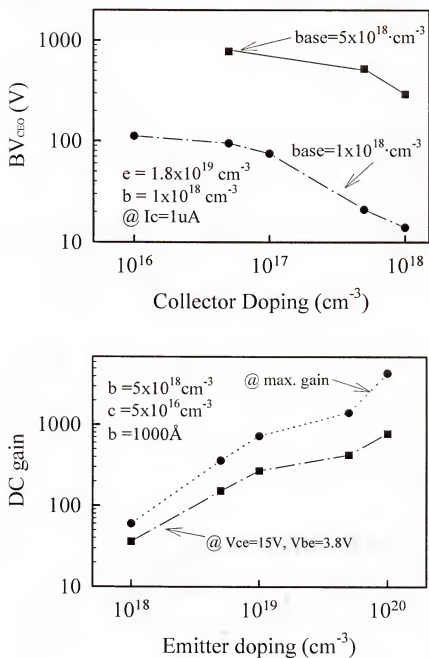


Fig. 4-23. BV_{CEO} (top) and dc current gain (bottom) as a function of emitter doping.

4.5. Rf Performance Of GaN-Based npn Bipolar Transistors

4.5.1. Experimental Methods

A schematic of the basic devices structure is shown in Figure 4-24. The effects of emitter stripe width, collector and base mesa width and spacing of the emitter and base metals were studied. The reference structure employed for the simulations consisted of a GaN emitter doped at $n=5 \times 10^{19} \text{ cm}^{-3}$, $0.15 \mu\text{m}$ thick and $1.8 \mu\text{m}$ in mesa width; a GaN base doped at $p=10^{19} \text{ cm}^{-3}$, $0.1 \mu\text{m}$ thick and $3.0 \mu\text{m}$ mesa width and finally a collector doped at $n=10^{17} \text{ cm}^{-3}$, $0.5 \mu\text{m}$ thick with a $4.2 \mu\text{m}$ mesa width. The junctions were assumed to be abrupt.

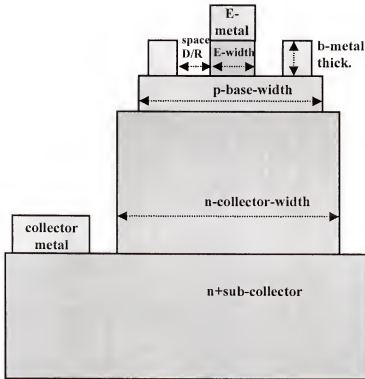


Fig.4-24. Schematic of BJT structure

The MEDICI code was used to simulate the dc and rf performance. The model includes field-dependent mobility, bandgap narrowing due to heavy doping, surface Auger recombination, Shockley-Reed-Hall statistics and also Boltzman transport theory. The output data included dc current gain, BV_{CEO} , f_T and Gummel plots.

4.5.2 Results and Discussion

Figure 4-25 shows simulated current flow contours at biasing conditions of $V_{CE}=12V$ and $V_{BE}=3.5V$ for the basic BJT structure with small emitter stripe width ($0.5\mu m$). Similar contours were obtained with narrower collector width (close to $1.5\mu m$), so that scaling does not appear to be a problem for the GaN BJT.

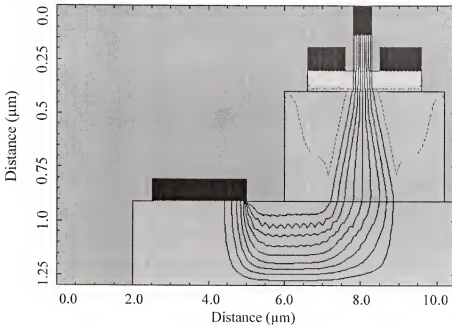


Fig.4-25. Current flow contours in GaN BJT at $V_{CE}=12V$, $V_{BE}=3.5V$.

The effect of layer material is shown in Figure 4-26 for $\text{In}_{0.2}\text{Ga}_{0.8}\text{N}$, GaN or $\text{Al}_{0.2}\text{Ga}_{0.8}\text{N}$ BJT's. The turn-on voltage increase with bandgap, as expected and dc current gains greater than unity are only achieved for biases above $\sim 2.5\text{V}$ for InGaN, $\sim 2.7\text{V}$ for GaN and $\sim 3.3\text{V}$ for AlGaN, as seen in the Gummel plots. It is expected that the wider the bandgap, the higher the maximum temperature and power of operation. At this stage only GaN material has displayed acceptable doping and purity characteristics to consider BJT fabrication.

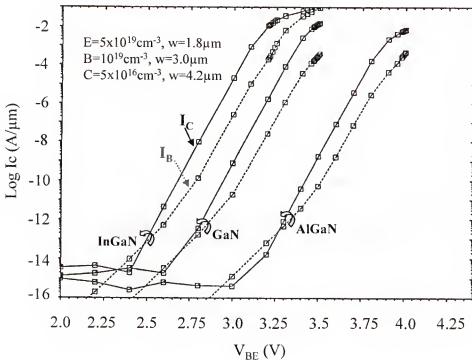


Fig. 4-26. Gummel plots for 1000Å thickness base, 1.8μm width emitter mesa, 3μm wide base mesa, 4.2μm wide collector mesa with respective doping of $5 \times 10^{19} \text{cm}^{-3}$, 10^{19}cm^{-3} , $5 \times 10^{16} \text{cm}^{-3}$ for different materials.

The BJT dc current gains expected from these simulated Gummel plots are shown as a function of collector current in Figure 4-27. As expected, the gain scales with decreasing bandgap. For a BJT, the common-emitter gain can be represented as ⁽⁷⁷⁾

$$\beta \approx \frac{D_n N_{DE} X_E}{D_p N_{AB} W} \approx \frac{I_C}{I_B}$$

where $D_{n,p}$ are the diffusion coefficients of electrons and holes respectively, $N_{DE,AB}$ are the donor or acceptor concentrations in the emitter and base, respectively, X_E is the width of the emitter region and W is the base width. In the low injection region, β will increase with I_C and the emitter injection efficiency will be the limiting factor determining the common-emitter gain. Under high injection conditions the gain decreases because the number of electrons injected into the base exceeds the Gummel number (ie the total number of acceptors in the base region, $N_A \cdot W$) and also because of carrier injection into the collector region and the related shift of the high field region from the emitter-base junction into the collector region, ie., the Kirk effect. This occurs when the collector current density, I_C , exceeds the saturation current density J_{SC} . ⁽⁷⁷⁾

$$\frac{I_C}{S} > J_{SC} = q \cdot N_{DC} \cdot v_s$$

where S is the device active area, q is the electron charge, N_{DC} is the donor concentration in the collector and v_s is the carrier saturation velocity. These effects are seen from Figure 4-27 to become important at current densities above $\sim 10^{-2} \text{ A} \cdot \mu\text{m}^{-2}$. Another factor limiting common-emitter current gain at high current levels can be related to the base resistance between the central section of the transistor and the base contact, which leads to emitter current crowding.

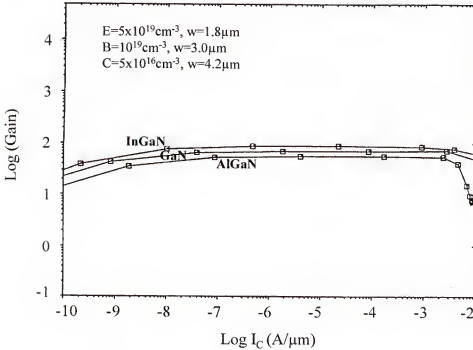


Fig. 4-27. DC current gain as a function of collector current for the BJTs described in Figure 4-26.

Figure 4-28 shows simulated common-emitter characteristics for the GaN BJT for base levels of $5 \times 10^{18} \text{ cm}^{-3}$ (top) or $5 \times 10^{17} \text{ cm}^{-3}$ (bottom). The latter condition leads to an absence of saturation, through the very low charged carriers in GaN base showing in the I-V characteristics. Punch-through between emitter to collector layers happened at lower V_{CE} comparing to the $5 \times 10^{18} \text{ cm}^{-3}$ condition (top). This emphasizes the need for achieving high base doping levels for acceptable bipolar junction transistors or heterojunction bipolar transistor operation.

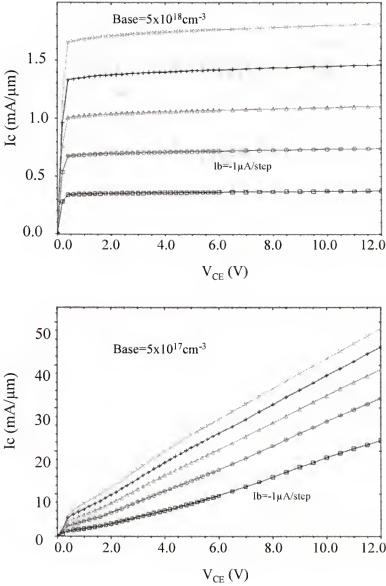


Fig. 4-28. Common-emitter characteristics for GaN BJT with base doping of either $5 \times 10^{18} \text{ cm}^{-3}$ (top) or $5 \times 10^{17} \text{ cm}^{-3}$ (bottom).

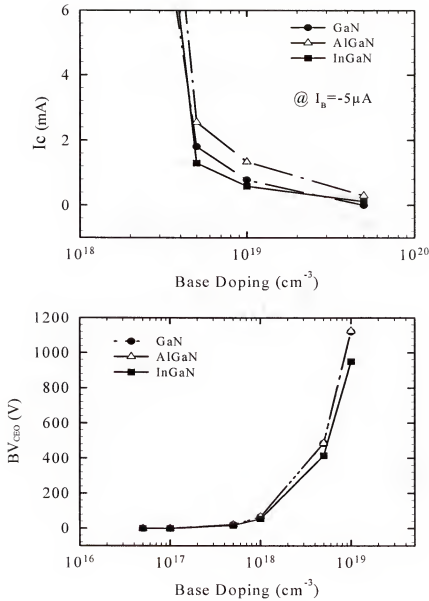


Fig. 4-29. Saturated I_C (top) and BV_{CEO} (bottom) as a function of base doping for GaN BJT with 1000Å thick base, emitter doping $5 \times 10^{19} \text{ cm}^{-3}$ and collector doping ($5 \times 10^{16} \text{ cm}^{-3}$).

Figure 4-29 shows saturation collector current at a base current of 5μA (top) and BV_{CEO} (bottom), as a function of base doping for the reference structure with GaN, AlGaIn or InGaIn as the component materials. There is not a strong dependence of either parameter or material type. At low base doping the base is fully depleted at zero bias, leading to the observed dependences shown in Figure 4-29.

The breakdown voltage of the collector-emitter junction BV_{CE} is related to that of the collector-base junction BV_{CB} through the equation ⁽⁷⁷⁾

$$BV_{CE} = BV_{CB}(1 - \alpha)^{\frac{1}{mb}}$$

where α is the common-base current gain and mb is a constant that depends on the doping profile in the collector and on temperature. This relation can be rewritten as ⁽⁷⁷⁾

$$BV_{CEO} = \frac{\epsilon \cdot BV_{CB}^2}{2qN_{DC}} \cdot (1 - \alpha)^{\frac{1}{mb}}$$

where ϵ is the permittivity of GaN, E_{BR} is the breakdown field strength and N_{DC} is the donor concentrations in the collector. Figure 4-30 shows the effect of collector thickness (top) and base thickness (bottom) on BV_{CEO} for different materials comprising the basic BJT structure. Once again this parameter increases with bandgap, as expected.

The cut-off frequency, f_T for a bipolar transistor can be expressed as ⁽⁷⁷⁾

$$f_T = \frac{g_m}{2\pi(C_{BE} + C_{BC})}$$

where f_T is defined as the frequency at which the short-circuit common-emitter current gain drops to unity, g_m is the transconductance and $C_{BE,BC}$ are the junction capacitances

of base-emitter and base-collector, respectively. The equation for f_T can also be represented as ⁽⁷⁷⁾

$$f_T \approx \frac{g_m}{2\pi\tau_{eff}}$$

where τ_{eff} is the effective transit time. Figure 4-31 shows the dependence of f_T and dc gain on base doping (top) and collector doping (bottom). Note that $f_T \geq 100$ GHz with a gain of ~ 800 for a base doping level of $5 \times 10^{18} \text{ cm}^{-3}$.

The effects of base thickness and base mesa width on f_T are shown in Figure 4-32. The magnitude of f_T is a very strong function of base capacitance, with very thin layers ($< 500 \text{ \AA}$) needed to keep $f_T > 100$ GHz. The cut-off frequency was much less dependent on base mesa width, for a fixed emitter mesa width of $0.5 \mu\text{m}$.

Finally, Figure 4-33 shows the influence of both emitter to base-metal spacing (top) and emitter mesa width (bottom) on f_T . At very short metal spacing the cut-off frequency is reduced, while it saturates for values of $\geq 0.5 \mu\text{m}$. These are important trends to understand when designing the BJT devices structure for high frequency operation.

In summary and conclusions, the base to emitter metal spacing, base doping and base thickness are found to dominate the rf performance of GaN BJTs. The low ionization efficiency of Mg acceptors in the base is a major limitation on BJT performance through its influence on base resistance. Future work will examine the relative tradeoff of using pnp devices, where base resistance is less of a problem and also of the expected high temperature performance of npn BJTs.

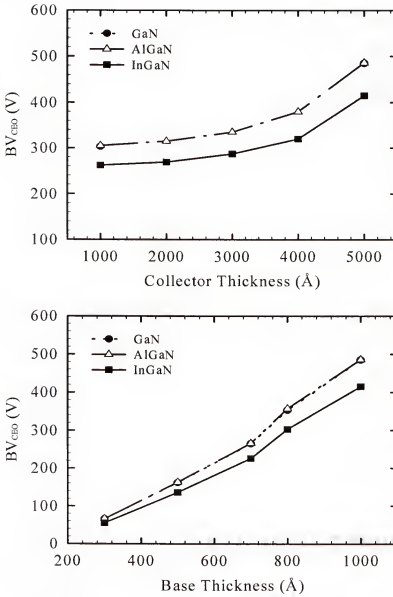


Fig. 4-30. BV_{CEO} as a function of either collector (top) or base (bottom) thickness. The base doping is $5 \times 10^{18} \text{ cm}^{-3}$ emitter doping $5 \times 10^{19} \text{ cm}^{-3}$ and collector doping $5 \times 10^{16} \text{ cm}^{-3}$.

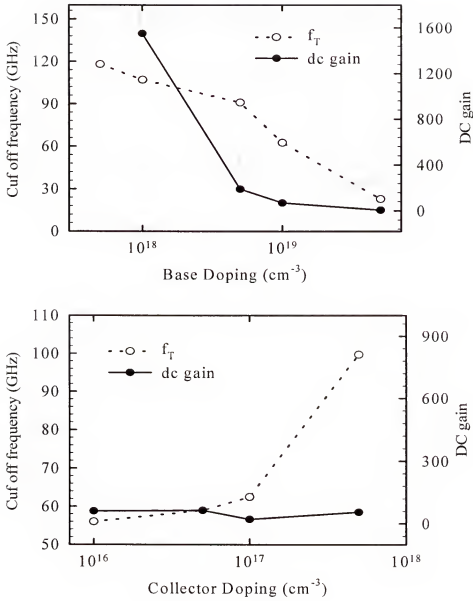


Fig. 4-31. f_T and dc current gain as a function of base (top) or collector (bottom) doping. The base is 1000Å thick in both cases.

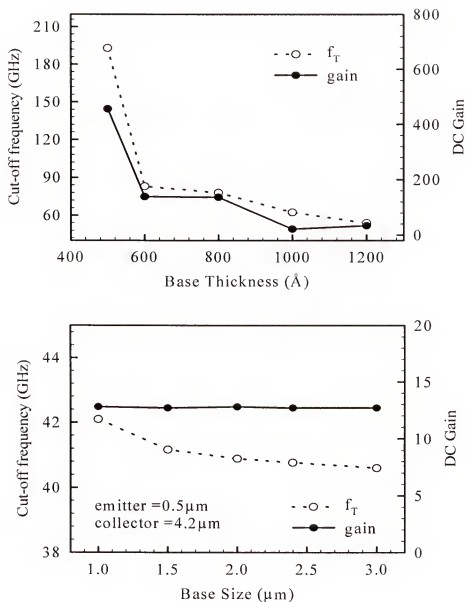
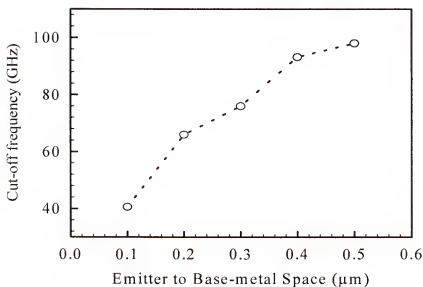


Fig. 4-32. f_T versus base thickness (top) or base mesa size (bottom) for GaN BJT with emitter doping $5 \times 10^{19} \text{ cm}^{-3}$, collector doping 10^{17} cm^{-3} , base doping 10^{19} cm^{-3} , emitter size 0.5 μm and collector size 4.2 μm.

GaN BJT



GaN BJT

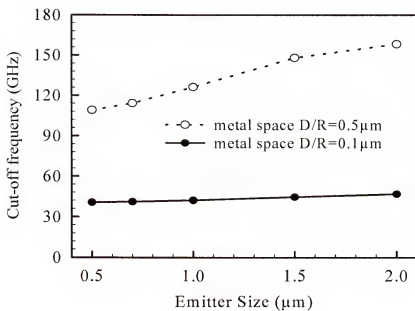


Fig.4-33. f_T versus emitter to base metal space (top) or emitter size (bottom) for GaN BJT with emitter doping 10^{19}cm^{-3} , base width $3\mu\text{m}$ and collector size $4.2\mu\text{m}$.

CHAPTER 5 SIMULATION OF GaN-BASED PNP BIPOLAR TRANSISTORS

5.1. Introduction

Recent improvements in growing p-type InGaN (hole concentration near 10^{19} cm^{-3}) have renewed interest in developing pnp GaN-based heterojunction bipolar transistor (HBTs) and bipolar junction transistors (BJTs).^(40, 42, 78-79) In the pnp configuration the problems of having a resistive base that plagues the realization of npn bipolar devices are eliminated because the base is now n-type and can be heavily doped with shallow silicon donor (ionization energy 20meV). Only a few reports have appeared on the experimental and theoretical performance of pnp HBTs and BJTs. The most promising of these was achievement of a common-emitter current gain of 50 at 25°C for a pnp GaN BJT.⁽⁴⁰⁾

In this chapter we report on the temperature characteristics of GaN/AlGaIn HBTs, using electrical device simulations. The devices are predicted to exhibit cut-off frequency, f_T , up to 45 GHz for 0.5μm emitter dimensions, compared to >150 GHz for npn structures. The pnp structure may offer some solution to the problems of the npn devices caused high base resistance and contact resistance.^(1-39, 40-42, 45, 78, 79)

5.2. Temperature Dependence of pnp GaN/InGaIn HBT Performance

5.2.1. Experimental Methods

The reference structure consisted of a 0.5μm thick GaN collector doped at $5 \times 10^{16} \text{ cm}^{-3}$ (4μm length), a 0.1 μm thick InGaIn base doped at 10^{18} cm^{-3} (3μm length) and an 0.15μm thick GaN emitter doped at 1 or $5 \times 10^{19} \text{ cm}^{-3}$ (0.5μm length). The p-type dopant

was assumed to be Mg with an ionization level of 170 meV while the n-type dopant was Si with an ionization level of 20 meV. The dc current gain, cut-off frequency (f_T), collector current (I_C), Gummel plots, and collector-emitter breakdown voltage (BV_{CEO}) were achieved from the MEDICI simulation using the conditions reported previously.⁽⁴⁵⁾ Figure 5-1 shows the basic 0.5 μm small size emitter and InGaN base HBT structure that was simulated.

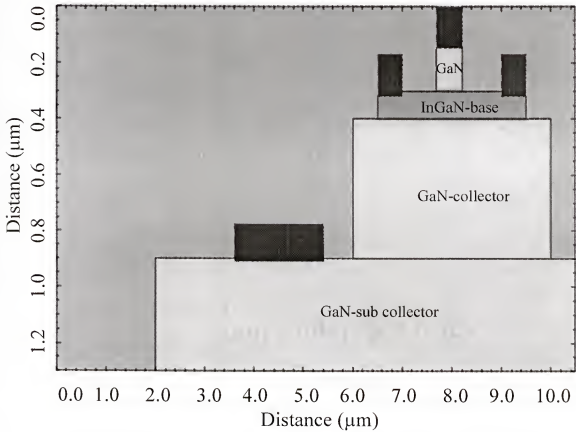


Fig. 5-1. Schematic of simulated HBT structure

5.2.2. Results And Discussion

The major effect of operating temperature is increased ionization efficiency of the Mg acceptors. The hole concentration, p , is related to the acceptor ionization energy (E_A) and temperature T through

$$P \propto \exp\left(\frac{-E_A}{kT}\right)$$

where k is the Boltzmann's constant. As temperature is increased, the sheet resistance of the layers will decrease and contact resistance will also be reduced. An example is shown in the simulated common-emitter characteristics of Figure 5-2, where the temperatures are either 473 K (top) or 673 K (bottom). Note the much reduced initial slope of the I-V characteristics at 673 K due to the lower contact resistance.

The higher hole concentration in the emitter and collector also produce a significant enhance in the Gummel plots. Figure 5-3 shows the plots at either 300 K (top) or 700 K (bottom). Note the much higher current levels and smaller turn-on voltage at 700 K. This is a characteristic of wide bandgap bipolar transistors, in that their performance improves with increasing temperature. Major limitations to date include the poor ohmic contacts combined with high leakage currents. A Gummel plot is taken with base and collector shorted to reduce effects from impact ionization in the collector and from collector-base leakage current. If the base contact has non-ohmic character and there is significant junction leakage, the Gummel plot may give an unrealistic measure of dc current gain. As the current is increased, the effect of leakage current is decreased and the measured current gain more truly represents the intrinsic performance of the HBT.

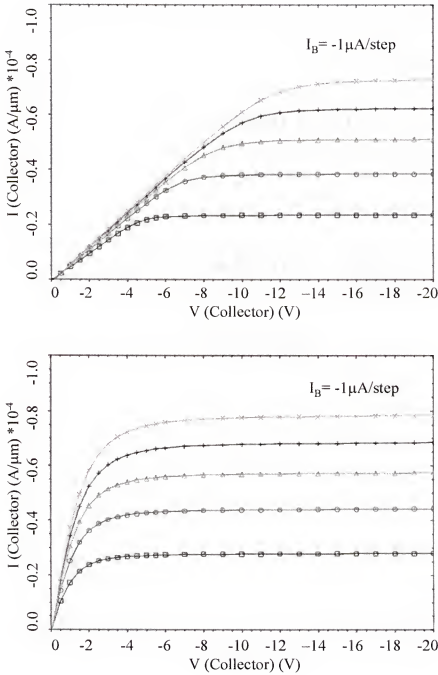


Fig. 5-2. Common-emitter characteristics at 473 K (top) and 673 K (bottom) of GaN/InGaN HBT.

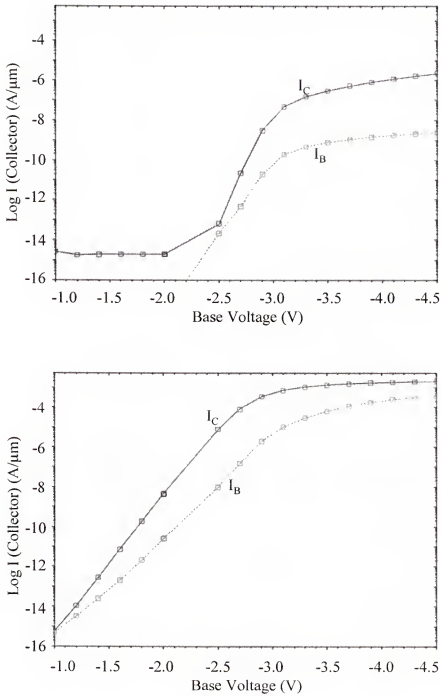


Fig. 5-3. Gummel plots at 300 K (top) and 700 K (bottom) of GaN/InGaN HBT with $V_{\text{CE}} = -12$ V

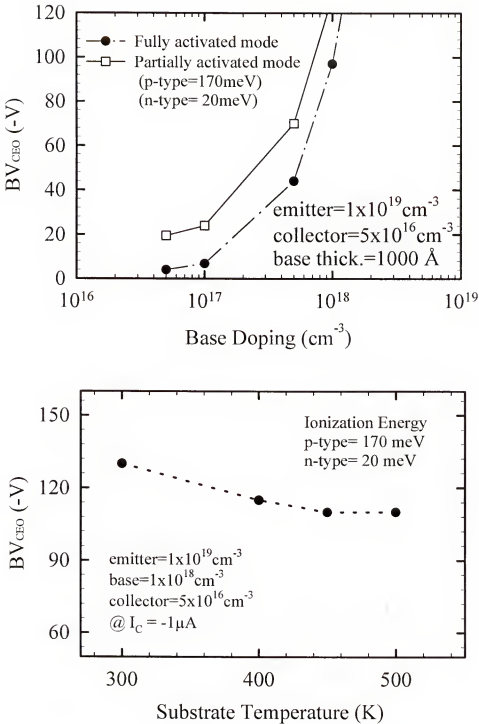


Fig. 5-4. BV_{CEO} versus base doping (top) and temperature (bottom) at a collector current of $-1 \mu\text{A}$. In the former case both completely ionized and partially ionized acceptors in the structure are shown. The emitter doping was 10^{19} cm^{-3} .

Incomplete ionization also effects the junction breakdown voltages through the influence on carrier concentration. Figure 5-4 (top) shows the effect of partial ionization on BV_{CEO} , relative to what would be expected for complete ionization. The latter case corresponds to operation at very high temperatures ($> 500^{\circ}\text{C}$). This data was converted into a plot of BV_{CEO} versus temperature, as shown in Figure 5-4 (bottom). The decrease in BV_{CEO} is relatively small ($< 20\%$) over the temperature range 300-500 K.

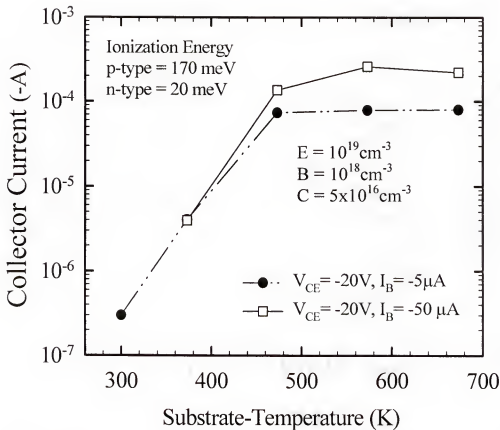


Fig. 5-5. I_C as a function of temperature for $V_{CE} = -20\text{ V}$ and $I_B = -5$ or $-50\text{ }\mu\text{A}$.

The collector current is shown for two different base current levels over the temperature range 300-700K in Figure 5-5, assuming partial ionization of the Mg acceptors with 170meV. The I_C values only saturate for the particular biasing conditions above temperatures of ~ 450 K. At room temperature the collector current is so low that it could be dominated by junction leakage. These curves can be used to indicate practical high operating temperatures for the GaN/InGaN HBTs.

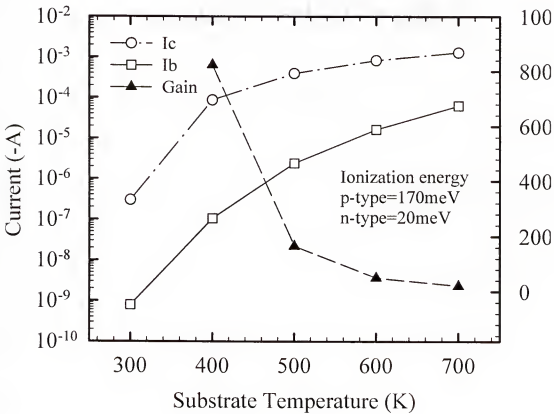


Fig. 5-6. I_C , I_B and gain as a function of temperature for $V_{CE} = -12$ V, $V_{BE} = -3.5$ V, emitter doping of $5 \times 10^{19} \text{ cm}^{-3}$ and base thickness 1000 Å.

The temperature dependence of I_C , I_B and current gain is shown for Figure 5-6 at $V_{CE} = -12$ V and $V_{BE} = -3.5$ V. For operating temperatures > 500 K, the current gain is in the range $\sim 10 - 120$. Since I_B increases faster than I_C , the gain decreases with increasing operating temperature.

The cut-off frequency, f_T , for an HBT can be represented ⁽⁷⁷⁾

$$f_T = \frac{g_m}{2\pi(C_{BE} + C_{BC})}$$

where g_m is the transconductance and C_{BE} , C_{BC} are the junction capacitances of base-emitter and base-collector, respectively. The f_T values are inversely dependent on the effective carrier transit times. Figure 5-7 shows the variation of f_T with temperature for $-40V_{CE}$ bias level. The data clearly shows that pnp GaN/InGaN HBTs will be capable of reasonable increase temperature at elevated temperatures. At room temperature the f_T value are too small to be useful.

In summary and conclusions, pnp GaN/InGaN HBTs offer numerous advantages over npn configurations, in particular this structure gets around the limitations of high base resistance that plagues npn devices. A drift-diffusion model shows that $0.5\mu\text{m}$ emitter dimension pnp GaN/InGaN HBTs should exhibit f_T up to 50 GHz at 700 K, with dc current gains > 10 at this temperature. The GaN/InGaN system appears to be the most promising of all the nitride heterostructures for elevated temperature microwave power application requiring high linearity.

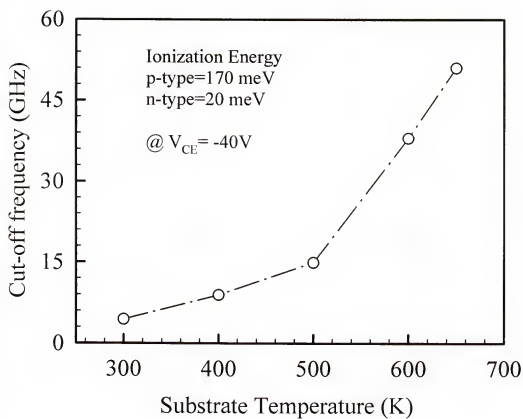


Fig. 5-7. f_T versus temperature for emitter doping $5 \times 10^{19} \text{ cm}^{-3}$, $V_{CE} = -40 \text{ V}$.

CHAPTER 6

SUMMARY

In summary, a self-aligned process for small-area GaN-based HBTs and GaN BJTs with regrown base or emitter layers has been developed. To improve the metal Ohmic contact on p-base region, carbon high doped GaAs thin layer was regrown on base contact region also. Further work is needed on mask alignment, surface morphology, etch selectivity and device yield in addition to improvements in material quality.

The temperature dependent performance of large and small-area GaN/AlGaIn HBTs has been measured. The dc current gain is found to improve with temperature. These results are analyzed in terms of improved base resistance. A highly resistive base layer induced by the deep Mg nature forces base current flowing directly to the collector, bypassing the base. These carriers are usually required to control the amount of the base-emitter bias, and the amount of electron injection from the emitter to the base. Hence, reducing the free hole carrier concentration in the base has a direct impact on the current collected at the collector.

For the HBT simulation, the effects of base layer structure on the predicted performance of GaN HBTs was investigated using a drift-diffusion model. The use of AlGaIn/GaN superlattices did not produce working devices for any of the conditions we employed. However InGaIn/GaN superlattices, double or single layer bases all showed practical dc performance when employed in GaN HBTs. Grading of the InGaIn composition was found to provide higher dc current gains than constant equivalent

compositions in the InGa_N. Under these conditions, the choice of emitter materials (AlGa_N or Ga_N) or emitter doping were not strong factors in influencing current gain.

The low ionization efficiency of Mg acceptors in the Ga_N base, which controls the hole concentration and therefore the base resistance, is shown to have important effect on AlGa_N/Ga_N HBT performance through its influence in the base thickness needed to avoid depletion of this layer. Gains of several hundred are predicted at room temperature for practical doping levels.

The base to emitter metal spacing, base doping and base thickness are found to dominate the rf performance of Ga_N devices also. Future work will examine the relative tradeoff of using pnp devices, where base resistance is less of a problem and also of the expected high temperature performance of npn BJTs.

The effects of layer doping and thickness on the predicted performance of Ga_N/In_{0.2}Ga_{0.8} HBTs has been investigated using a drift-diffusion model. The InGa_N base device is found to be attractive from a number of viewpoints including higher base conductivity and less sensitivity of gain on base thickness compared to AlGa_N/Ga_N structures. It is still necessary to achieve good quality ohmic contacts and minimize junction leakage in order to have acceptable common-emitter characteristics.

Finally, pnp Ga_N/InGa_N HBTs offer numerous advantages over npn configurations, in particular this structure gets around the limitations of high base resistance that plagues npn devices. A drift-diffusion model shows that 0.5 μ m emitter dimension pnp Ga_N/InGa_N HBTs should exhibit f_T up to 50 GHz at 700 K, with dc current gains >10 at this temperature. The Ga_N/InGa_N system appears to be the most

promising of all the nitride heterostructures for elevated temperature microwave power application requiring high linearity.

REFERENCES

1. L.S. McCarthy, P. Kozodoy, M. Rodwell, S.P. DenBaars, M.Rodwell and U.K. Mishra, IEEE Electron. Dev. Lett. EDL-20 277 (1999).
2. F.Ren, C.R.Abernathy, J.M.Van Hove, P.P.Chen, R.Hickman, J.J.Klaassen, R.F. Kopf, H.Cho, K.B.Jung, J.LaRoche, R.G.Wilson, J.Han, R.J.Shul, A.G.Baca and S.J.Pearton, MRS Internet J. Nitride Semicond. Res. 3 41 (1998).
3. R.M.Asbeck, E.T.Yu, S.S.Lau, W.Sun, X.Dang and C.Shi, Solid-State Electron. 44 211 (2000).
4. F.Ren, J.Han, R.Hickman, J.M.Van Hove, P.P.Chow, J.J.Klaassen, J.R.LaRoche, K.B.Jung, H.Cho, X.Cao, S.M.Donovan, R.F.Kopf, R.G.Wilson, A.G.Baca, R.J.Shul, L.Zhang, C.G.Willison, C.R.Abernathy and S.J.Pearton, Solid-State Electron. 44 239 (2000).
5. J.Han, A.G.Baca, R.J.Shul, C.G.Wilson, L.Zhang, F.Ren, G.Dang, A.P.Zhang, S.M.Donovan, X.Cao, K.B.Jung, H.Cho, C.R.Abernathy, S.J.Pearton and R.G.Wilson, Appl. Phys. Lett. 74 2702 (1999).
6. E.Alekseev and D.Pavlidis, Solid-State Electron. 44 245 (2000).
7. D.J.H.Lambert, D.E.Lin and R.D.Dupuis. Solid-State Electron. 44 253 (2000).
8. R.Hickman, J.M.VanHove, P.P.Chow, J.J.Klaassen, A.M.Wowchack, C.J.Polley, D.J.King, F.Ren, C.R.Abernathy, S.J.Pearton, K.B.Jung, H.Cho and J.R.LaRoche, Solid-State Electron. 44 377 (2000).
9. C.Monier, F.Ren, J.Han, D.C.Chang, R.J.Shul, K.P.Lee, A.Zhang, A.G.Baca and S.J.Pearton, IEEE Trans Electron, Dev, 48 427 (2001).
10. B.S.Shelton, D.J.H.Lambert, J.J.Huang, M.M.Wong, L.Chowdhury, T.G.Zhu, H.K.Kwon, J.C.Weber, M.Benarama, M.Feng and R.D.Dupuis, IEEE Tran Electron. Dev. 48 490 (2001).
11. L.S.McCarthy, I.Smorchkova, H.Xing, D.Kozodoy, D.Fini, J.Limb, D.Pulfrey, J.S.Spek, M.J.W.Rodwell, S.P.Denbars and U.K.Mishra, IEEE Tran Electron. Dev. 48 543 (2001).
12. D.L.Pulfrey and S.Fathpour, IEEE Tran Electron. Dev. 48 597 (2001).

13. S.J.Pearnton, J.C.Zolper, R.J.Shul and F.Ren, J.Appl. Phys. 86 (1999).
14. X.A.Cao, G.T.Dang, A.P.Zhang, F.Ren, J.M.VanHove, J.Klaassen, C.J.Rolley, A.M.Wowchack, P.P.Chow, D.J.King, C.R.Abernathy and S.J.Pearnton, Solid-State Lett. 3 144 (2000).
15. X.Cao, J.M.Van Hove, J.J.Klaassen, C.J.Polley, A.M.Wowchack, P.P.Chow, D.J.King, F.Ren, G.Dang, C.Monier, S.J.Pearnton and F.Ren, Solid-State Electron. 44 649 (2000).
16. X.Cao, J.M.Van Hove, J.J.Klaassen, C.J.Polley, A.M.Wowchack, P.P.Chow, D.J.King, A.P.Zhang, G.Dang, C.Monier, S.J.Pearnton and F.Ren, Solid-State Electron. 44 1255 (2000).
17. X.Cao, J.M.Van Hove, J.J.Klaassen, C.J.Polley, A.M.Wowchack, P.P.Chow, D.J.King, A.P.Zhang, G.Dang, C.Monier, S.J.Pearnton and F.Ren, Solid-State Electron. 44 1261 (2000).
18. A.P.Zhang, G.T.Dang, F.Ren, J.Han, A.G.Baca, R.J.Shul, H.Cho, C.Monier, X.A.Cao, C.R.Abernathy and S.J.Pearnton, Appl. Phys. Lett. 76 2943 (2000).
19. C.Monier, S.J.Pearnton, P.C.Chang, A.G.Baca and F.Ren, Appl. Phys. Lett 76 3115 (2000).
20. X.A.Cao, G.T.Dang, A.P.Zhang, F.Ren, C.R.Abernathy, S.J.Pearnton, J.M.VanHove, J.Klaassen, C.J.Rolley, A.M.Wowchack, P.P.Chow, D.J.King and S.N.G.Chu, Electrochem. Solid-State Lett. 3 333 (2000).
21. S.J.Pearnton, F.Ren, A.P.Zhang and K.P.Lee, Mat. Sci. Eng. R30 55 (2000).
22. G.D.Dang, B.Luo, A.P.Zhang, X.Cao, F.Ren, S.J.Pearnton, H.Cho, W.S.Hobson, J.Lopata, J.M.VanHove, P.P.Chow and D.J.King, Solid-State Electron. 44 2097 (2000).
23. K.P.Lee, A.P.Zhang, G.Dang, F.Ren, J.Han, S.N.G.Chu, W.S.Hobson, J.Lopata, C.R.Abernathy, S.J.Pearnton and J.W.Lee, Solid-State Electron. 45 243 (2000).
24. A.P.Zhang, J.Han, F.Ren, K.E.Waltrip, C.R.Abernathy, B.Luo, G.Dang, J.W.Johnson, K.P.Lee and S.J.Pearnton, Electroche. Solid-State Lett. 4 639 (2000).
25. K.P.Lee, A.P.Zhang, G.Dang, F.Ren, J.Han, W.S.Hobson, J.Lopata, C.R.Abernathy, S.J.Pearnton and J.W.Lee, J.Vac.Sci. Technol. A19 1878 (2000).

26. S.J.Pearnton, F.Ren, A.P.Zhang, G.Dang, X.Cao, K.P.Lee, H.Cho, B.Gila, J.W.Johnson, C.Monier, C.R.Abernathy, J.Han, A.G.Baca, J.I.Chai, C.M.Lee, T.E.Nee, C.Chuo and S.N.G.Chu, *Mat. Sci. Eng.* B82 227 (2001).
27. L.Chernyak, A.Osisky, S.J.Pearnton and F.Ren, *Electronics Lett.* 37 1411 (2001).
28. A.P.Zhang, G.T.Dang, F.Ren, J.Han, C.Monier, A.G.Baca, X.A.Cao, H.Cho, C.R.Abernathy and S.J.Pearnton, *Solid-State Electron.* 46 933 (2002).
29. A.P.Zhang, F.Ren, T.J.Anderson, C.R.Abernathy, R.K.Singh, D.H.Holloway, S.J.Pearnton, D.Palmer and G.E.McGuire, *Critical Rev. Solid-State Mat. Sci.* 27 1 (2002).
30. J.B.Limb, L.McCarthy, P.Kozodoy, H.Xing, J.Ibbetson, Y.Smorchova, S.P.Den Baars and U.K.Mishra, *Electronics, Lett.* 35 1671 (1999).
31. B.S.Shelton, J.J.Huang, D.J.Lambert, T.G.Zhu, M.M.Wong, C.J.Eiting, H.K.Kwon, M.Feng and R.D.Dupuis, *Electron. Lett.* 36 80 (2000).
32. S.Yoshida and J.Suzuki, *J.Appl. Phys.* 85 7931 (1999).
33. S.Yoshida and J.Suzuki, *J.Appl. Phys.* 38 L851 (1999).
34. Y.Zhang, C.Cai and P.P.Ruden, *Mat. Res. Soc. Symp.* 622 TG-25.1 (2000).
35. J.J.Huang, M.Hattendoof, M.Feng, D.J.Lambert, B.S.Shelton, M.Wong, U.Chowdhury, T.G.Zhu, H.K.Kwon and R.D.Dupuis, *Electron Lett.* 36 1239 (2000).
36. T.Makimoto, K.Kamahara and N.Kobayashi, *Phys. Stat. Sol. A.* 188 183 (2001).
37. J.J.Huang, M.Hattendoof, M.Feng, D.J.Lambert, B.S.Shelton, M.M.Wong, U.Chowdhury, T.G.Zhu, H.K.Kwon and R.D.Dupuis, *IEEE Electron. Dev. Lett.* 22 157 (2000).
38. J.J.Huang, D.Caruth, M.Feng, D.J.Lambert, B.S.Shelton, M.Wong, U.Chowdhury, T.G.Zhu, H.K.Kwon and R.D.Dupuis, *Electron Lett.* 37 393 (2001).
39. L.S.McCarthy, I.Smorchova, P.Fini, M.J.W.Rodwell, J.Speck, S.P.DenBaars and U.K.Mishra, *Electron Lett.* 38 144 (2002).
40. K.Kumahura, T.Makimoto and N.Kobayashi, *Appl. Phys. Lett.* 80 1225 (2002).
41. H.Xing, S.Keller, Y.F.Wu, L.McCarthy, I.P.Smorchkova, D.Buttari, R.Coffie, D.S.Green, G.Parish, S.Heikman, L.Sheng, N.Zhang, J.Xu, B.Keller, S.DenBaars and U.K.Mishra, *J. Phys. C.* 13 7139 (2001).

42. T.Makimoto, K.Kumahura and N.Kobayashi, Appl. Phys. Lett. 79 380 (2000).
43. T.Makimoto, K.Kumashash and N.Kobayashi, Jap. J. Appl. Phys. 39 L195 (2000).
44. H.Xing, D.Jena and U.K.Mishra, IEEE Electron. Dev. Lett. (in press).
45. K.P.Lee, A.Dabiran , P.P.Chow, S.J.Pearton and F.Ren , Solid-State Electron 47 969 (2003).
46. I.D.Goepfert, E.F.Schubert, A.Osinsky, P.E.Norris and N.M.Faller, J.Appl. Phys. 81 2030 (2000).
47. A.Polyalkov, N.B.Smirnov, A.V.Govorkov, A.V.Osinky, P.E.Norris, S.J.Pearton, J.Van Hove, A.Worwchack and P.Chow Appl. Phys. Lett. 79 4373 (2000).
48. Manasreh, "III-V Nitride Semiconductors: Electrical, Structural and Defects Properties, 2000".
49. H.Amos, M.Kito, K.Hiramatsu and I.Akasaki, Jpn.J.Appl. Phys. 28, L2112, 1989.
50. Y.Kato, S.Kitamura, K.Hiramatsu, N.Sawaki, J. Cryst. Growth 144, 133 (1994).
51. M.A. Littlejohn, J.R. Hauser, T.H. Glisson, Appl. Phys. Lett. 26, 625 (1976).
52. B. Gelmont, K. Kim, M. Shur, J. Appl. Phys. 74, 1818 (1993).
53. S.K. O'Leary, B.E. Fortz, M.S. Shur, U. Bhaphkar, L.F. Eastman, J. Appl. Phys. 83, 826 (1998).
54. B.E. Fortz, S.K. O'Leary, M.S. Shur, L.F. Eastman, U.V. Bhaphkar, Proc. MRS 512, 549 (1998).
55. M. Shur, B. Gelmont, M.A. Khan, J.Electron. Mater. 25, 777 (1996).
56. B.E. Fortz, S.K. O'Leary, M.S. Shur, L.F. Eastman, Proc. MRS 512, 555 (1998).
57. R. Gaska, J.W. Wang, A.Osinsky, Q. Chen, M.A. Khan, A.O. Orlov, G.L. Snider, M.S. Shur, Appl. Phys. Lett. 72, 707 (1998).
58. N.G. Weimann, L.F. Eastman, D. Doppalapudi, H.M. Ng, T.D. Moustakas, J. Appl. Phys. 83, 3656 (1998).
59. X. Zang, P. King, D. Walker, J. Piotrowski, A. Roalski, A. Saxler, Appl. Phys. Lett. 67, 2028 (1995).

60. R.J. Radtke, U. Waghmare, H. Ehrenreich, C.H. Grein, Appl. Phys. Lett. 73, 2087 (1998).
61. X. Zhang, D.H. Rich, J.T. Kobayashi, P.D. Dapkus, Appl. Phys. Lett. 73, 1430 (1998).
62. Z.Z. Bandic, P.M. Bridger, E.C. Piquette, T.C. McGill, Appl. Phys. Lett. 73, 3276 (1998).
63. M.E.Levinshtein, S.L.Rumyantsev, M.S.Shur, Properties of Advanced Semiconductor Material (Wiley Interscience, New York, 2001).
64. M.S. Shur and M.A. Khan, MRS. Bull. 22 (2), 44 (1997).
65. U.V. Bhapkar and M.S. Shur, J. Appl. Phys., 82 (4), 1649 (1997).
66. S. K. O'Leary, B. E. Foutz, M. S. Shur, U. V. Bhapkar, and L. F. Eastman, Solid State Comm. 105, 621 (1998).
67. Avant Cooperation, Medici manual, Two-Dimensional Device Simulation, Version 2001.4, (Freemont, CA, 2003).
68. R. Klima, Three Dimensional Device Simulation with MINIMOS-NT, 1998, http://www.iue.tuwien.ac.at/reviews/1998/.text/klima_text.html, 6/6/2003.
69. Stanford University, TCAD software PISCES-2ET, <http://www-tcad.stanford.edu/tcad.html>, 9/6/2003.
70. M. Vanzi, Sedan semiconductor device analysis, 1997, <http://www.eeng.brad.ac.uk/help/.packlangtool/.ecad/.sedan.html>, 9/12/2003.
71. J.S. Yuan and J.J. Liou, Semiconductor Device Physics and Simulation (Plenum Press, New York, 1998).
72. K.A. Jackson, Compound Semiconductor Devices Structures and Processing (Wiley-VCH, Weinheim Germany, 1998).
73. P.A. Houston, high-frequency heterojunction bipolar transistor device design and technology, electronics & communication engineering journal, 221. Oct. (2000).
74. B.S. Shelton, J.J. Huang, D.J. Lambert, T.G. Zhu, M.M. Wong, C.J. Eiting, H.K. Kwon, M. Feng and R.D. Dupuis, Electron. Lett. 36 27 (2000).
75. Y.Zhang, C.Cai and P.P.Ruden, J.Appl. Phys. 88 1067 (2000).

76. J.H. Edgar and H. Amamo, Properties of GaN Group III-nitrides (INSPEC, IEE, London, 2000).
77. M.S. Shur, Physics of Semiconductor Devices (Prentice-Hall, Englewood Cliffs, NJ 1990).
78. K. Kumahura, T. Makimoto and N. Kobayashi, J. Appl. Phys. 39 L337 (2000).
79. K. Kumahura, T. Makimoto and N. Kobayashi, J. Cryst. Growth 221 267 (2000).

BIOGRAPHICAL SKETCH

Kyu-pil Lee was born in the Republic of Korea on May 28, 1961, and he is a Christian. He received his B.S. degree in materials science and engineering from Han Yang University in Seoul, Korea, in 1985 and his M.S degree in materials science and engineering from the University of Florida in Gainesville, Florida, in 2000.

He joined the Semiconductor Research and Development Center of Samsung Electronics Company in Kiheung Kyunggi-Do Korea in 1985. Since then he has worked as an architect for the development of CMOS technology and products, such as the 1Mb, 4Mb, 16Mb, 64Mb, 256Mb, 1Gbits, SOI-based CMOS memory devices and Low Voltage Battery Operation (LVBO) memory devices. In 1997, Samsung awarded him best engineer for developing 1Giga-bit Dynamic Random Access Memory (1Gb DRAM) one of the world's first, and the excellent Patent Award for his R&D patent work for the Samsung.

His publication is extensive and includes over 50 journal papers and over 40 conference papers. Also he has received over 45 Korean patents, over 20 US, 12 Japanese, and several German, French, Italian and Taiwan patents for his original inventions in the field.

His credentials have earned him a place among the most influential individuals. Likewise, he is listed in Who's Who in America, Who's Who in Science and

Technologies, International Who's Who, Strathmore's Who's Who, International WHO's WHO of professional and Korean Biographical Dictionary respectively.

He joined the University of Florida for his Ph.D. program as part of the Samsung Human Resource Cultivation Program in 1998, and he is focusing on the development of Heterojunction Bipolar Transistors (HBTs) using wide band gap materials such as GaN-based materials.

He is interested in spintronic devices using magnetic materials for next generation memory devices. After finishing his program at the University of Florida, he will return to Samsung to work.

I certify that I have read this study and that in my opinion it conforms to acceptable standards of scholarly presentation and is fully adequate, in scope and quality, as a dissertation for the degree of Doctor of Philosophy.



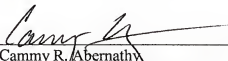
Stephen J. Pearton, Chair
Professor of Materials Science and
Engineering

I certify that I have read this study and that in my opinion it conforms to acceptable standards of scholarly presentation and is fully adequate, in scope and quality, as a dissertation for the degree of Doctor of Philosophy.



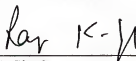
Fan Ren
Professor of Chemical Engineering

I certify that I have read this study and that in my opinion it conforms to acceptable standards of scholarly presentation and is fully adequate, in scope and quality, as a dissertation for the degree of Doctor of Philosophy.



Cammy R. Abernathy
Professor of Materials Science and
Engineering

I certify that I have read this study and that in my opinion it conforms to acceptable standards of scholarly presentation and is fully adequate, in scope and quality, as a dissertation for the degree of Doctor of Philosophy.



Rajiv K. Singh
Professor of Materials Science and
Engineering

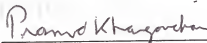
I certify that I have read this study and that in my opinion it conforms to acceptable standards of scholarly presentation and is fully adequate, in scope and quality, as a dissertation for the degree of Doctor of Philosophy.



David Norton
Professor of Materials Science and
Engineering

This dissertation was submitted to the Graduate Faculty of the College of Engineering and to the Graduate School and was accepted as partial fulfillment of the requirements for the degree of Doctor of Philosophy.

December 2003



Pramod P. Khargonekar
Dean, College of Engineering

Winfred M. Phillips
Dean, Graduate School